



HAL
open science

Hydroacoustic Study of a Seismic Swarm in 2016–2017 near the Melville Transform Fault on the Southwest Indian Ridge

Vaibhav Vijay Ingale, Sara Bazin, Jean-Arthur Olive, Anne Briaais, Jean-Yves Royer

► **To cite this version:**

Vaibhav Vijay Ingale, Sara Bazin, Jean-Arthur Olive, Anne Briaais, Jean-Yves Royer. Hydroacoustic Study of a Seismic Swarm in 2016–2017 near the Melville Transform Fault on the Southwest Indian Ridge. *Bulletin of the Seismological Society of America*, 2023, 113 (4), pp.1523 - 1541. 10.1785/0120220213 . hal-04225291

HAL Id: hal-04225291

<https://hal.univ-brest.fr/hal-04225291v1>

Submitted on 21 Nov 2023

HAL is a multi-disciplinary open access archive for the deposit and dissemination of scientific research documents, whether they are published or not. The documents may come from teaching and research institutions in France or abroad, or from public or private research centers.

L'archive ouverte pluridisciplinaire **HAL**, est destinée au dépôt et à la diffusion de documents scientifiques de niveau recherche, publiés ou non, émanant des établissements d'enseignement et de recherche français ou étrangers, des laboratoires publics ou privés.



Distributed under a Creative Commons Attribution - NonCommercial 4.0 International License

1 **Hydroacoustic study of a seismic swarm in 2016-2017 near Melville Transform Fault on the**
2 **Southwest Indian Ridge**

3

4 **Authors:** Vaibhav Vijay Ingale¹, Sara Bazin¹, Jean-Arthur Olive², Anne Briais¹, and Jean-Yves
5 Royer¹

6 **Emails:** vaibhavvijay.ingale@univ-brest.fr ; sara.bazin@univ-brest.fr ; olive@geologie.ens.fr ;
7 anne.briais@univ-brest.fr ; jean-yves.royer@univ-brest.fr

8 **Affiliation:**

9 ¹Lab Geo-Ocean, University of Brest, CNRS, Ifremer, UMR6538, F-29280, Plouzané, France

10 ²Laboratoire de Géologie, CNRS - École Normale Supérieure, PSL University, Paris, France

11

12 **Corresponding author:** vaibhavvijay.ingale@univ-brest.fr

13

14 **Abstract**

15 Hydroacoustic monitoring has become particularly efficient for studying the low-
16 magnitude seismicity occurring at mid-ocean ridges. In 2016-17, a seismic swarm occurred near
17 the Melville transform fault of the ultraslow-spreading Southwest Indian Ridge in the Indian
18 Ocean. It comprised 258 events in the land-based International Seismological Centre catalog,
19 extending from June 2016 to March 2017. We examined this seismicity using hydroacoustic
20 records from 3 to 9 hydrophones moored in the Southern Indian Ocean, from the OHASISBIO
21 temporary network and the International Monitoring System of the Comprehensive Nuclear-Test-
22 Ban Treaty Organization. We detected 27624 hydroacoustic events spanning 298 days (June 01,
23 2016 – March 25, 2017) with lower localization and origin time errors. These include several

24 energetic, short-duration impulsive events, which we interpret as due to lava-water interactions on
25 the seafloor. The spatio-temporal distribution of all the detected events shows an absence of clear
26 tectonic mainshock-aftershock sequence and indicates a magmatic origin of the swarm with bursts
27 of seismic activity caused by dike emplacements.

28

29 **Key points:**

- 30 1. Analysis of hydroacoustic T-waves associated with the seismicity near the Melville
31 transform fault
- 32 2. Detection of energetic impulsive events, which are associated with lava-water interaction
33 on the seafloor
- 34 3. Spatio-temporal distribution of earthquakes caused by dike emplacements and stress-
35 readjustment

36

37 **Introduction**

38 Along mid-ocean ridges (MORs) or divergent boundaries separating tectonic plates, the
39 oceanic lithosphere is created by a complex interplay of magmatic and tectonic processes, which
40 result in numerous earthquakes that have been investigated since the 1970s (e.g., Sykes, 1970;
41 Bergman and Solomon, 1990; Tolstoy et al., 2001; Rundquist and Sobolev, 2002; Tolstoy and
42 Bohnenstiehl, 2006; Schlindwein et al., 2015; Yu et al., 2018). The associated low-level seismicity
43 is generally lacking in records from land-based seismic networks due to the remoteness of MORs
44 and the rapid attenuation of seismic waves in the solid Earth (Fox et al., 2001; Korger and
45 Schlindwein, 2012). Since the late 1980s, local studies using ocean-bottom seismometers (OBS;
46 e.g., Toomey et al., 1985; Wolfe et al., 1995; Tolstoy et al., 2008; Yu et al., 2021) and regional

47 studies using autonomous underwater hydrophones (e.g., Fox et al., 1995; Smith et al., 2003;
48 Bohnenstiehl et al., 2008; Royer et al., 2015) have greatly contributed to a comprehensive
49 understanding of MOR seismicity. This is possible because low-frequency hydroacoustic T-waves
50 from seismic events propagate over long distances with little attenuation within the ocean's low-
51 velocity waveguide, known as the Sound Fixing and Ranging (SOFAR) channel (Tolstoy and
52 Ewing, 1950; Weston and Rowlands, 1979; Fox and Squire, 1994). Earthquakes excite T-waves
53 in the water column through the conversion of seismic waves into acoustic waves at the seafloor
54 (Fox et al., 1995, 2001; Dziak et al., 2012; Jamet et al., 2013). T-wave detection studies provide
55 insights into magmato-tectonic processes and transform fault dynamics over large sections of
56 MORs (Dziak et al., 1997; Bohnenstiehl et al., 2002; Smith et al., 2002; Bohnenstiehl et al., 2003;
57 McGuire et al., 2005; Olive and Escartín, 2016; Giusti et al., 2018; Parnell-Turner et al., 2022).
58 This is the reason why the OHASISBIO network of hydrophones was set up in 2010 to
59 simultaneously monitor the three Indian Ocean ridges with contrasting spreading rates (Royer,
60 2009). This long-term network has captured 15 swarms since 2010 (e.g., Tsang-Hin-Sun et al.,
61 2016; Ingale et al., 2021), particularly along the Southwest Indian Ridge (SWIR). This paper
62 focuses on the strongest, longest and most recent swarm on the SWIR.

63 The ultraslow-spreading SWIR, with a full spreading rate of ~ 14 mm/a (Cannat et al., 1999;
64 Chu and Gordon, 1999), is a major spreading ridge that has separated Africa from Antarctica for
65 over 100 Ma (Patriat et al., 1997). It extends from the Bouvet Triple Junction (BTJ) in the southern
66 Atlantic Ocean to the Rodrigues Triple Junction (RTJ) in the Indian Ocean (Figure 1; Royer et al.,
67 1988, 1989). Its western end (BTJ) is older than its eastern end (RTJ) due to the lengthening and
68 eastward propagation of the ridge axis at the RTJ (Patriat and Ségoufin, 1988). It is characterized
69 by several large-offset transform faults that divide the ridge into spreading segments of varying

70 lengths (Mendel et al., 1997) with several magmatic and amagmatic ridge segments (Dick et al.,
71 2003) marked by a deep axial valley bounded by ~3 km-high ridges (Sauter and Cannat, 2010).
72 The cyclic nature of volcanic construction and tectonic dismemberment across the SWIR has
73 shaped its rugged morphology (Mendel et al., 2003).

74 The Melville Transform Fault (TF) offsets the SWIR axis to the north by ~150 km (Parson
75 et al., 1997) and marks a boundary between two sections of the SWIR in terms of offset,
76 segmentation, bathymetry, seafloor structure, crustal thickness, magma supply, mantle
77 temperature and seismicity distribution (Patriat et al., 1997; Baines et al., 2007). West of the
78 Melville TF (60°45'E), the SWIR shows an obliquity of 40° and contains several long-lived
79 transform and non-transform discontinuities (Figure 1). The section east of the Melville TF and up
80 to RTJ (70°E) has an obliquity of 25° and is continuous with minor discontinuities. Also, segments
81 east of the Melville TF have a less regular pattern of Mantle Bouguer gravity anomalies (MBA),
82 compared with segments west of it (Rommevaux-Jestin et al., 1997). This observation can be
83 explained by a quasi-amagmatic spreading of the SWIR east of the Melville TF, with multiple
84 detachment faults exhuming mantle rocks and scarce volcanic constructions (Sauter et al., 2004).
85 The along-axis depth profile near the Melville TF shows striking variations with bathymetric highs
86 shallower than 3000 m adjacent to axial depth maxima (valley) deeper than 6000 m. Next to this
87 transform fault valley, the obliquity of the ridge axis reaches 40° at 61°25'E. It also shows a
88 spectacular bathymetric high near 61°25'E with peak-to-trough relief reaching 3700 m and a depth
89 gradient of up to 130 m/km (Patriat et al., 1997). East of this bathymetric high, the rift valley is
90 oblique and continuous up to 63°30'E, with depths ranging between 4500 and 5500 m (segment
91 14 in Cannat et al., 1999). This segment has a large-amplitude MBA low and its gravity signature

92 is broader than the topography, which can be interpreted as thick crust and/or reduced density crust
93 or mantle (Cannat et al., 1999).

94 Several seismic studies have been conducted along the SWIR, both east and west of the
95 Melville TF, based on teleseismic observations (e.g., Wiens and Petroy, 1990), hydroacoustic
96 observations (e.g., Tsang-Hin-Sun et al., 2016), or local OBS surveys (e.g., Yu et al., 2018; Schmid
97 et al., 2017). West of the Melville TF, a teleseismic analysis recorded seismicity associated with
98 an along-axis melt flow mechanisms (Läderach et al., 2012). East of the Melville TF, several short-
99 term OBS surveys interpreted the observed seismicity as magma movement related to diking
100 episodes (Schlindwein and Schmid, 2016; Meier and Schlindwein, 2018). In the vicinity of the TF
101 (Figure 1), between June 2016 and March 2017, there was a series of 258 earthquakes reported by
102 the International Seismological Centre (ISC; ISC, 2022; triangles in Figure 2) among which 17
103 events are reported in the Global Centroid Moment Tensor catalog (GCMT; Ekström et al., 2012;
104 diamonds in Figure 2). All of the latter show double-couple normal faulting mechanisms, 16
105 parallel to the SWIR axis and one parallel to the Melville TF.

106 To investigate this seismic series from the low-level seismicity lacking in the land-based
107 catalogs due to their detection threshold, we examined hydroacoustic data (T-waves) recorded by
108 autonomous hydrophones moored on either side of the SWIR from the OHASISBIO network
109 (Royer, 2009). The OHASISBIO (Hydroacoustic Observatory of the Seismicity and Biodiversity
110 in the Indian Ocean) is a long-term hydroacoustic program for monitoring the seismic activity
111 (e.g., Tsang-Hin-Sun et al., 2016) and the vocal activity of large marine mammals in the southern
112 Indian Ocean (e.g., Samaran et al., 2013; Leroy et al., 2017). The network is maintained during
113 the yearly voyages of R/V *Marion Dufresne* to the French Sub-Antarctic Islands. Along with the
114 OHASISBIO network, we also examined hydroacoustic data from the International Monitoring

115 System (IMS) of the Comprehensive Nuclear-Test-Ban Treaty Organization (CTBTO). This
116 global network is designed to detect sounds generated by underwater explosions (Okal, 2001;
117 Gibbons, 2022). Since the seismicity near the Melville TF is located within the OHASISBIO and
118 CTBTO network, observed hydroacoustic events are likely to have more accurate locations than
119 the events from the ISC catalog. Since the hydrophones are more sensitive to low-magnitude
120 events, we detected 27624 events (circles in Figure 2), i.e., ~107 times more than in the ISC catalog
121 (258). The detailed analysis of this improved and dense catalog of hydroacoustic events helps to
122 understand the nature of seismicity near the Melville TF.

123

124 **Data and Methods**

125 In comparison with seismic wave propagation in the solid Earth, sound waves propagate
126 in the ocean through a more homogeneous oceanic sound-velocity channel. For this reason,
127 hydroacoustic data provide a remarkable improvement in the detection threshold (Fox et al., 1994)
128 as well as location accuracy (Fox et al., 2001; Bohnenstiehl and Tolstoy, 2003) of seismic events,
129 compared to distant land-based seismic networks. In this study, we analyzed data from
130 hydrophones of the OHASISBIO network (Figure 1) that are moored in the SOFAR channel axis
131 at depths ranging from 1000 m to 1300 m (Table 1). The hydrophones are located south of La
132 Réunion Island (MAD-W, MAD and MAD-E), north-east and south-west of Amsterdam Island
133 (NE-AMS and SW-AMS3), south of the Southeast and Southwest Indian ridges (S-SEIR and S-
134 SWIR), and west and south of Kerguelen Island (WKER2 and ELAN). All sites had a single
135 hydrophone except the SW-AMS, which had a triad of 3 hydrophones. These hydrophones were
136 all set to record acoustic waves continuously at a rate of 240 Hz on 3-byte-long samples. Both
137 before deployment and after recovery, their high-precision clocks are synchronized with a GPS

138 clock to account for the instrument clock-drift (in the range of 0.002 to 0.100 ppm; Table 1).
 139 Among these sites, the hydrophone at MAD was operational from June 2016 to December 2016.
 140 In the SW-AMS triad of hydrophones, only SW-AMS3 was operational between June 2016 and
 141 November 2016. In January 2017, the SW-AMS triad was replaced by a single hydrophone and
 142 the MAD site was no longer operational. However, other sites like MAD-W, MAD-E, NE-AMS
 143 and S-SWIR started operating at this time. In the entire duration (June 2016 to March 2017)
 144 WKER2 and S-SEIR sites recorded data without any significant intermission.

145 In the Indian ocean, IMS-CTBTO hydrophones are located ~180 km northwest (H08N)
 146 and ~25 km south (H08S) of Diego Garcia Island, ~100 km southwest off Cape Leeuwin, Australia
 147 (H01W), and ~30 km north (H04N) of Crozet Island (Figure 1 inset). All these sites comprise a
 148 triad of hydrophones also moored in the SOFAR channel and deployed in a triangular
 149 configuration with ~2 km spacing between instruments. They are similarly set to record acoustic
 150 waves continuously at a rate of 250 Hz with a 24-bit A/D resolution. For this study, we only used
 151 one hydrophone from the H08S triad (H08S1) and from the H01W triad (H01W1). We could
 152 neither use the H04N triad since it started recording after May 2017 nor the H08N one because it
 153 is situated north of the Chagos Bank, which blocks T-waves originating from the Melville TF.

154 **Table 1:** Locations and acquisition parameters of the hydrophones of the OHASISBIO and CTBTO networks

| Sites | MAD-W | MAD | MAD-E | S-SEIR | NE-AMS | SW-AMS3 | WKER2 | S-SWIR | H08S1 | H01W1 |
|--------------------|----------|----------|----------|----------|----------|----------|----------|----------|----------|----------|
| Latitude [°S] | 29.051 | 26.084 | 24.197 | 33.514 | 31.575 | 42.989 | 46.602 | 38.550 | 7.645 | 34.893 |
| Longitude [°E] | 54.260 | 58.140 | 63.010 | 70.867 | 83.241 | 74.850 | 60.547 | 52.879 | 72.474 | 114.154 |
| Water depth [m] | 1280 | 1260 | 1180 | 1210 | 2760 | 1160 | 980 | 1150 | 800 | 800 |
| Sampling rate [Hz] | 240 | 240 | 240 | 240 | 240 | 240 | 240 | 240 | 250 | 250 |
| Sensitivity [dB] | -163.4 | -163.7 | -163.5 | -163.5 | -163.5 | -168.6 | -163.6 | -163.3 | -165.2 | -165.2 |
| Start Time | 06/01/17 | 29/01/16 | 08/02/17 | 25/01/16 | 07/02/17 | 21/01/16 | 12/01/16 | 08/01/17 | 01/01/16 | 01/01/16 |
| End Time | 06/01/18 | 08/02/17 | 13/02/18 | 11/02/18 | 13/02/18 | 09/12/18 | 04/02/18 | 22/12/17 | 31/12/17 | 31/12/17 |
| Clock drift [ppm] | -0.1004 | -0.0393 | -0.0466 | -0.0021 | -0.0466 | -0.0162 | -0.0080 | -0.0205 | N/A | N/A |

155

156 The data from these hydrophones were simultaneously analyzed with the “Seas” software
157 developed at the NOAA Pacific Marine Environment Laboratory (Fox et al., 2001) and processed
158 as described in Royer et al., (2015). Each earthquake was located after manually picking the
159 highest energy in the T-wave spectrograms (Figure S1; Schreiner et al., 1995; Slack et al., 1999).
160 If two events originate from the same location at different times (> 40 s), or if two events occur at
161 the same time at different locations, the energy arrivals will be distinct (and “pickable”) on all
162 hydrophones due to the spread of the network. Once T-waves were identified on three or more
163 hydrophones, the source location and origin time in UTC were estimated by trial and error using a
164 non-linear least square minimization of the arrival times (Fox et al., 2001). Sound velocities in the
165 ocean were based on the three-dimensional and seasonal Global Digital Environment Model
166 (GDEM) at a resolution of 30 arc-minutes in latitude and longitude (Teague et al., 1990); then the
167 distances and arrival times on each hydrophone were calculated and averaged along great circles
168 joining the sources to each of the receivers. The errors in the latitude, longitude and origin time
169 were estimated from the covariance matrix of this least square minimization, weighted by the mean
170 square of the residuals.

171 Hydroacoustic events are characterized by their acoustic magnitude or Source Level (SL)
172 of the T-waves. The SLs are derived from the Received Levels (RL) at each hydrophone and
173 corrected for the transmission loss (TL) between the event and the hydrophone locations. The TL
174 accounts for the cylindrical sound-spreading loss between the event location and the hydrophone,
175 as well as the spherical sound-spreading loss in the water column between the seafloor acoustic
176 radiator and the sound channel axis (e.g., Jensen et al., 1994). The RL, expressed in decibels with
177 respect to 1 micro-Pascal at 1 meter (dB re μ Pa at 1 m, hereinafter dB), corresponds to the
178 maximum peak-to-peak amplitude in a 10s time-window centered on the peak of energy in the

179 acoustic signal, in the 3-110 Hz frequency range, which closely resembles the definition of seismic
180 magnitudes. The RLs are calculated in the 5-60 Hz frequency range, which is optimal for T-wave
181 spectra. This simple RL calculation is performed as the arrival times are picked, and is thus
182 convenient when processing large amounts of data. For the sake of comparison, it is also consistent
183 with previous studies by the PMEL or our group. Methods taking into account scattering effects
184 due to bathymetry or based on T- phase envelopes are perhaps more physically realistic, but require
185 more post-processing and thus are limited to the analysis of small datasets (Yang and Forsyth,
186 2003).

187 All the OHASISBIO hydrophone are equipped with HTI-90U sensors with similar
188 sensitivities near -163.5 dB, provided by the manufacturer, except at site SW-AMS3, equipped
189 with a HTI-04ULF sensor with a sensitivity of -168.6 dB (Table 1). Due to this difference in
190 sensitivity, the RLs on SW-AMS3 hydrophone differ greatly from that at all other sites. As an
191 example, for some representative events, the median RL was 98.5 ± 2.8 dB on MAD, 102.4 ± 2.6
192 dB on S-SEIR, 108.3 ± 2.9 dB on WKER2, whereas it was 131.2 ± 3.9 dB on SW-AMS3 (Figure
193 S2a). After correcting these RLs for the transmission loss, SLs for these events detected using all
194 4 stations was 230.9 ± 3.9 dB, whereas it was 211.1 ± 1.9 dB for the same events picked without
195 SW-AMS3, resulting in a difference of 19.8 dB (Figure S2b). So, instead of recomputing all the
196 SLs to account for this sensitivity discrepancy, we simply reduced them by 19.8 dB when the
197 events were picked using SW-AMS3 until November 28, 2016 (when it failed). Since the same
198 sensor was redeployed at SW-AMS in January 2017, the SLs were also corrected by the same
199 amount (19.8 dB) when SW-AMS was used in the triangulation.

200 The hydroacoustic catalog (hereinafter OHA) was built in a two-iteration process. In the
201 first iteration, we manually picked T-wave arrivals in a window size of 30 minutes and constructed

202 a catalog with the following information: the event ID; the number and names of hydrophones
203 used to locate the event; its latitude, longitude and SL; the 1σ uncertainties in latitude, longitude,
204 origin time and SL. In the second iteration, this information was used to zoom-in on the events in
205 a 10-minute time-window to manually re-pick the arrival times and relocate the hydroacoustic
206 events with a higher precision. This step improved the locations and times of the OHA events by
207 reducing the errors in latitude, longitude and origin time by ~ 8 -fold. In the first iteration, the
208 median errors were 2.88 km in latitude, 2.90 km in longitude and 0.90 s in origin time (Figure
209 S3a); in the second iteration, the error improved to 0.38 km, 0.38 km and 0.11 s, respectively
210 (Figure S3b). These errors are calculated only for events recorded by at least four hydrophones.
211 Out of a total of 27624 detected events, only 2095 events (7.5%) were located using three
212 hydrophones (between November 28, 2016 and January 06, 2017) and the remaining 25529 events
213 were located using four or more hydrophones.

214 The detection threshold of the hydrophone network is defined by the SL of completeness
215 (SL_c) which is derived from the frequency-size distribution of the acoustic events (Bohnenstiehl et
216 al., 2002). It can be compared to the magnitude of completeness of seismic events from land-based
217 catalogs. This is based on the assumption that acoustic events follow Gutenberg-Richter's law
218 (Gutenberg and Richter, 1954), where SLs would be proportional to the logarithm of the
219 cumulative number of events:

$$220 \quad \log N = a - b SL \quad (1)$$

221 where N is the cumulative number of events with a source-level greater or equal to SL and
222 constants a and b are the intercept and the slope of the line fitting the distribution of events. For
223 the OHA catalog, the SL_c is 206.6 dB, coinciding with the peak of the normal distribution of SL.
224 The roll-off point of this Gutenberg-Richter's fitting (equation 1) was 14013 for the OHA catalog

225 (Figure 3a-b). The number of ISC events (258) related to this swarm would be too small for a
226 meaningful comparison, furthermore biased towards high magnitudes. We thus considered all ISC
227 events located along the SWIR (i.e., in a similar tectonic context of an ultra-slow spreading ridge)
228 for years 2010 to 2020. The geographical distribution of these events is shown in Figure S4. Still,
229 this collection only amounts to 1933 ISC events vs 27624 OHA events. The magnitude (*mb*) of
230 completeness of the 1933 ISC catalog events is $M_{c(ISC)} = 4.1$ *mb* and the event distribution still
231 remains biased towards high magnitudes. The equivalent magnitude of completeness for the OHA
232 catalog $M_{c(OHA)} = 3.3$ *mb* was estimated by extrapolating the frequency-size distribution with a b-
233 value = 2.98 from the ISC events up to the number of events defining SL_c (Figure 3c). This
234 magnitude of completeness is 0.8 *mb* better than $M_{c(ISC)}$ and demonstrates that hydrophone arrays
235 provide more complete information about the seismicity along remote mid-oceanic ridges than
236 land-based catalogs. The total number of events detected by the OHASISBIO and CTBTO
237 networks over 10 months at a single location (June 2016 – March 2017) are ~14 times bigger than
238 that detected by land-based networks over 10 years along the whole SWIR (2010-2020). Similar
239 approaches for comparing M_c and SL_c have been used for hydroacoustic events detected along
240 MORs (Bohnenstiehl et al., 2002; Pan and Dziewonski, 2005; Olive and Escartin, 2016; Tsang-
241 Hin-Sun et al., 2016). The b-value = 2.98 for the ISC catalog means that there is likely a deficit of
242 large events ($M_{c(ISC)} > 4.1$) relative to small ones. This deficit suggests that a $b=0.47$ slope for the SL
243 is representative of a volcanic context. Fitting the two Gutenberg-Richter distributions would yield
244 a relationship of $SL = 186.00 + 6.25$ *mb*, or conversely $mb = 193.58 + 7.98$ SL, similar to that
245 found by Pan and Dziewonski (2005).

246

247 **Results**

248 Based on the ISC catalog, the seismic activity started with an event of 4.2 *mb* on June 9,
249 2016 at 21:50 UTC (SL = 211.7 dB) followed by 257 events until March 25, 2017 with magnitudes
250 ranging between 3.2 *mb* (December 14, 2016 at 11:22) and 5.7 *mb* (January 29, 2017 at 16:42).
251 Such events have SLs between 201.5 and 222.5 dB after the RL corrections. During this period,
252 17 GCMT catalog events were also reported with magnitudes ranging between 4.8 Mw (August 5,
253 2016 at 10:43 and August 6, 2016 at 01:11) and 5.5 Mw (September 16, 2016 at 18:38) within the
254 same SL range (Figure 4a). We examined the available hydroacoustic records from June 1, 2016
255 to March 25, 2017 (298 days), yielding a total of 27624 events showing a 107-fold increase in
256 event count and with SLs ranging from 185.8 dB to 227.9 dB. The events between November 28,
257 2016 and January 20, 2017 were picked on all hydrophones except at the SW-AMS site; hence
258 their SL is not corrected. In these detections, 627 events showed anomalously high SL between
259 January 9 and January 20, 2017. Their median SL was 216.2 ± 6.0 dB, which was higher by 9.6
260 dB than the median SL of all hydroacoustic events. Here, events were localized using S-SWIR,
261 WKER2, S-SEIR and MAD-W stations of the OHASISBIO network. Such high SL is mainly due
262 to relatively high RL of 118.8 ± 7.3 dB at the S-SWIR site, compared with RL of 106.0 ± 2.3 dB
263 at WKER2, 101.1 ± 3.4 dB at S-SEIR and 100.9 ± 3.4 dB at MAD-W (Figure S5). The large
264 dispersion in RL recorded by station S-SWIR is probably caused by a high noise-level in the ocean
265 (storm induced) or to strumming noise since the mooring is located near the front of the deep
266 circumpolar Antarctic current (see Orsi et al., 1995; Rintoul et al., 2001). Data from the WKER2
267 mooring does not display such a noise level in the 0-20 Hz bandwidth (Figure S6) and is less prone
268 to strumming as it is located south of the main circumpolar current track.

269 Several peculiar events, clustered on the slopes of bathymetric highs, east of the Melville
270 TF at 61°25'E (Figure 5a), are energetic up to 50-60 Hz and of short duration (~10-15s) compared

271 with the ~200s T-wave duration for large earthquakes (such as those reported in the ISC catalog;
272 Figure 5b and 5c). We have detected 118 such events with SLs ranging between 199.4 and 225.1
273 dB. These signals were detected at the nearest (MAD at 621 km) as well at the farthest sites
274 (WKER at 1858 km) of the OHASISBIO network, however not by the CTBTO network, probably
275 due to its remoteness from the Melville TF. Hereinafter, we call them impulsive events and will
276 discuss them in detail further below.

277 The seismic activity rate was very mild between June 1 and June 8, 2016 with only 73
278 events and an average of 9 events per day (solid curve in Figure 4b). On June 9, 2016, the seismic
279 activity intensified with 143 events per day (E/D). We detected 2637 events between June 9 and
280 June 30, 2016, ranging between 1 event and 263 E/D. The activity rate increased on June 18 and
281 then on June 30, coinciding with the occurrence of a strong normal faulting GCMT event (June
282 30-12:20, $M_w = 5.1$, $SL = 213.7$ dB). In July, there were 4248 events with a frequency of 47 to
283 244 E/D. The time clustering of strong ISC and impulsive events coincided with bursts of seismic
284 activity during this period. At the end of July, there were no strong events and lesser hydroacoustic
285 activity. In August, 3638 events were detected with a frequency ranging from 43 to 254 E/D. A
286 normal faulting GCMT event occurred in early August (August 05-10:43, $M_w = 4.8$, $SL = 209.4$
287 dB), coincidentally with another burst of activity. Two similar events occurred a day later (August
288 06-01:11, $M_w = 4.8$, $SL = 210.6$ dB; August 06-12:23, $M_w = 4.9$, $SL = 212.4$ dB). A temporal
289 cluster of impulsive events also coincided with this burst of activity. Near the end of August, we
290 observed two normal faulting GCMT events (August 25-01:02, $M_w = 5.0$, $SL = 216.9$ dB and
291 August 27-08:59, $M_w = 5.0$, $SL = 218.3$ dB) and another burst in seismic activity. Then 4330
292 events were detected in September, with a minimum of 65 events and a maximum of 272 E/D. In
293 this period, greater seismicity rates coincided with the September 16-18:38, $M_w = 5.5$ event.

294 October 2016 displays the maximum monthly count of events in the entire duration, with a total
295 of 4787 events and rates ranging from 68 to 297 E/D. The maximum number of E/D (297) between
296 June 2016 and March 2017 was reached on October 11, 2016. In November, the cumulative
297 number of events flattened as the seismicity rate decreased with 3076 events and 57 to 220 E/D.
298 A seismic burst on November 10 coincided with a cluster of few impulsive and ISC events. Then
299 2040 events were detected in December with 13 to 193 E/D.

300 A new activity burst was observed on December 14, 2016 and another temporal clustering
301 of ISC events coincided with small burst of seismic activity on December 26, 2016. In January
302 2017, 1240 events ranged between 7 to 101 E/D. A few impulsive and ISC catalog events coincided
303 with another activity burst on January 07, 2017. After this, the seismicity gradually became milder;
304 however, it slightly increased at the end of January 2017 coinciding with the GCMT event (January
305 29-16:42, $M_w = 5.4$, $SL = 222.5$ dB) and a dense temporal cluster of impulsive events. In February,
306 1127 events were detected with a minimum of 11 events and a maximum of 77 E/D. One impulsive
307 event on February 16, 2017 coincided with another seismic activity burst. There was a normal
308 faulting event on February 21-11:08 ($M_w = 5.0$, $SL = 214.0$ dB), but the activity rate did not
309 increase after its occurrence. In March, there were only 428 events with daily occurrences between
310 1 and 33 events; the seismic activity gradually ended until March 25, 2017. Overall, despite the
311 observed variations in the seismic rate, the cumulative number of events (dashed curve in Figure
312 4b) gradually increased until November 10 and became flat after December 14, 2016. Such a long
313 and sawtoothed distribution of events does not resemble a single mainshock-aftershock sequence.

314 We computed the distance of the median location of all events per day from a reference
315 point (RP) at $29^{\circ}19'S$, $61^{\circ}04'E$ (cross in Figure 2) to observe the average spatial distribution of
316 the events. The coordinate of the RP is the median location of all the events from the OHA catalog

317 and is situated on the downslope of bathymetric highs at $61^{\circ}25'E$, and south of the ridge axis
318 (Figure 2 inset). When it initiated, the seismicity was positioned at ~ 10 km from the RP with little
319 fluctuations (Figure 4c and Figure 6). After a temporal cluster of ISC and impulsive events between
320 June 09 and 16, the seismicity migrated back-and-forth between the transform valley and
321 bathymetric highs, showing a wider spatial distribution from June 19 to August 03, 2016. At the
322 time of higher activity on August 05 (Figure 4b), the events were focused within a ± 3 km area
323 located ~ 10 km from the RP. Then the events shifted by ~ 30 km away from the RP and migrated
324 back-and-forth between the valley and bathymetric highs within a ± 10 km wide area until
325 September 21, 2016. At this time, the events were ~ 60 km away from the RP and coincided with
326 a short episode of lower seismic activity rate between September and October 2016. Following it,
327 the seismicity rate was higher and the events focused within an area of ± 10 km, narrowing between
328 the transform valley and bathymetric highs until November 10, 2016. Furthermore, the events
329 densely focused in a narrow ± 2 km area around the RP, until January 20, 2017. Then, events
330 suddenly moved ~ 30 km away from the RP and formed a narrow band of seismicity (± 10 km)
331 aligned along the ridge axis until February 02, 2017. Afterwards, the events were randomly
332 distributed away from the RP until the seismicity ended.

333 **Discussion**

334 **Seismicity and lithospheric strength near Melville TF**

335 With an average temporal distribution of events of ~ 93 E/D over 298 days, this seismic
336 swarm is the strongest one reported along the SWIR in terms of duration and total number of events
337 (Schlindwein, 2012; Schmid et al., 2017; Yu et al., 2018). Hydroacoustic events from two other
338 SWIR seismic swarms have been studied previously using the OHASISBIO network: at segment
339 18 near Novara TF and at segment 4 near the RTJ (Ingale et al., 2021). Both swarms occurred in
340 2018 and lasted for a shorter duration compared with this one, the former comprising 1109 events
341 over 13 days (85 E/D) and the latter 4880 events over 33 days (148 E/D). The strong seismicity
342 near the Melville TF could result from distinct accretion processes along this section of the SWIR
343 axis, distinguishing it from the other two segments. The Melville TF was established at ~ 40 Ma,
344 time of the last major change in spreading direction of the SWIR (Patriat et al., 1997). The subaxial
345 crust and mantle beneath the Melville TF are cooler (Mendel et al., 1997), which is inferred from
346 greater positive anomalies of shear wave velocity in the upper mantle (Forsyth et al., 1987;
347 Debayle and L  v  que, 1997). This cooler mantle beneath the Melville TF results in a stronger
348 lithosphere with a thicker brittle layer, accommodating numerous earthquakes (Schlindwein and
349 Schmid, 2016; Grevemeyer et al., 2019) and an axial valley oblique to spreading. In this studied
350 seismic cluster, large-magnitude events (ISC and GCMT catalogs) are clustered near the axial area,
351 but the low-magnitude events are spread over a wider area and parallel to the ridge axis. The off-
352 axis lithosphere near the Melville TF might therefore be more accommodative to magmato-
353 tectonic seismicity (Rundquist and Sobolev, 2002).

354 **Short and energetic impulsive events**

355 The short duration, high-energy and frequency content suggest that impulsive events
356 (Figure 5) are H-waves (i.e., water borne), meaning that the energy is directly released into the
357 water column and does not travel into the solid crust as for regular T-waves (Bazin et al., 2022).
358 T-waves originating from shallow earthquakes would have a much broader (i.e., dispersed)
359 waveform due to the size of the seismic/acoustic conversion area; furthermore, its magnitude
360 should be significant to be detectable as far as 2000 km away (e.g., at WKER2), which is
361 incompatible with a shallow earthquake depth. Additionally, records of earthquakes detected at
362 the MAD site often display P-wave preceding T-wave arrivals by 240 – 280s (Figure S1) which
363 are not observed before impulsive signals. This confirms that the latter events are not due to
364 shallow earthquakes.

365 Hydroacoustic impulsive events have been observed at other spreading ridges (e.g.,
366 Schlindwein and Riedel, 2010; Tan et al., 2016; Caplan-Auerbach et al., 2017; Le Saout et al.,
367 2020) and underwater volcanoes (e.g., Chadwick et al., 2008; Green et al., 2013; Dziak et al., 2015;
368 Crone and Bohnenstiehl, 2019; Tepp et al., 2020; Tepp et al., 2019; Bazin et al., 2022; Saurel et
369 al., 2022). Tepp and Dziak, (2021) have gathered a complete review of the different source
370 mechanisms that could explain such events. Among them, the signature of impulsive signals from
371 our study resembles closely to those generated by lava water interaction when hot lava reaches
372 seafloor, similar as reported on the East Pacific Rise (e.g., Tan et al., 2016) and Juan de Fuca Ridge
373 (e.g., Caplan-Auerbach et al., 2017). The cabled array of the Ocean Observatories Initiative
374 recorded thousands of impulsive acoustic signals with SLs in the range of 130 - 190 dB during
375 Axial seamount eruption on the Juan de Fuca Ridge in 2015, which were interpreted as lava-water
376 interactions and also confirmed by a post eruption bathymetric survey (Le Saout et al., 2020).

377 During another volcanic eruption off Mayotte Island in 2020-2021, several impulsive events
378 featured SLs, duration and frequency range comparable to ours (Figure S7), and were interpreted
379 as hot lava and seawater interaction based on direct observation of active lava flows (Bazin et al.,
380 2022; Saurel et al., 2022). This result strengthens our interpretation of impulsive events near the
381 Melville TF being associated with hot lava-seawater interactions. In Le Saout et al. (2020) and
382 Bazin et al. (2022) studies, the hydrophones were less than 20 km from the Axial seamount and
383 about 50 km from the volcanic source off Mayotte Island, respectively. The discrepancy in SL as
384 well as in the number of impulsive events reported in these two studies vs. ours suggest that only
385 the strongest impulsive events (SL > 199 dB; Figure 4a) were captured by the OHASISBIO
386 hydrophones, the closest being 620 km away from their source.

387 Hydroacoustic impulsive events have been observed at other spreading ridges, but were
388 attributed to different source mechanisms (e.g., Le Saout et al., 2020; Tepp et al., 2019; Tepp and
389 Dziak, 2021). Some have been associated with bursting gas bubbles during magma rising
390 (Schlindwein and Riedel, 2010) or magma bubble bursts (Chadwick et al., 2008; Dziak et al.,
391 2015). In these studies, impulsive events were only recorded by very near stations (< 20 km)
392 compared with our observations (600-2000 km away). Along the East Pacific Rise and Axial
393 seamount on the Juan de Fuca Ridge, near hydrophones (< 20 km) recorded very short duration (<
394 1 s) impulsive events with dominant frequencies of ~22 Hz; they were interpreted as steam-bursts
395 associated with hot lava and seawater interaction at the seafloor (Tan et al., 2016; Caplan-Auerbach
396 et al., 2017). In recent volcanic eruptions off Mayotte Island in the western Indian ocean, impulsive
397 events showed a similar duration and frequency range as ours (Bazin et al., 2022; Figure S5). These
398 events were interpreted as hot lava and seawater interaction based on direct evidence of active lava
399 flows (Bazin et al., 2022; Saurel et al., 2022). This observation and waveform similarities lead us

400 to interpret the impulsive events near the Melville TF as hot lava seawater interactions. For the
401 same reason, events with the same waveform characteristics along the SWIR near Novara TF
402 (58°E) and Segment 4 (67.5°E), also detected as far as 2000 km away from their location, were
403 also interpreted as hot lava seawater interaction (Ingale et al., 2021).

404

405 **Temporal distribution of events and modified Omori's law**

406 A potential cause for the observed oscillatory pattern (Figure 4b) in the seismicity could
407 be the occurrence of several large tectonic events. Indeed, the decay in seismic activity after a main
408 shock can be characterized by a modified Omori's law (Utsu et al., 1995):

$$409 \quad n(t) = K(c + t)^{-p}, \quad (2)$$

410 where $n(t)$ is the frequency of aftershocks per unit time t . K , c and p are empirically derived
411 constants. K reflects the productivity of a mainshock and c represents the activity within the earliest
412 part of the sequence. The exponent p shows the aftershock sequence's decay rate. It reflects the
413 properties of the fault system (Mogi, 1967) and thermal state of the surrounding lithosphere
414 (Kisslinger and Jones, 1991; Bohnenstiehl et al., 2002; Klein et al., 2006). It ranges from 0.6 to
415 2.5 with a median of 1.1 based on a compilation of more than 200 aftershock sequences (Utsu et
416 al., 1995). For tectonic seismicity, p -values are generally found in the 0.8-1.2 range (Utsu, 1999;
417 Schmid and Grasso, 2012; Hainzl et al., 2016) and in the range of 0.9 - 1.2 for various aftershock
418 sequences observed along the oceanic TF (Davis and Frohlich, 1991; Bohnenstiehl et al., 2002).

419 After a visual inspection of the main changes in the slope of the cumulative distribution of
420 events as well as slope changes following the occurrence of strong ISC/GCMT events in a zoomed
421 temporal window (month-wise), we identified 12 sequences. Each sequence starts with a sudden
422 increase in seismicity rate, noted by a date and asterisk in Figure 4b, followed by a gradual

423 decrease. The duration of all sequences was determined till the number of events per hour reached
424 zero, i.e., the cumulative distribution of events became flat. Three out of 12 sequences (1, 2 and
425 9) were not triggered by a large earthquake recorded by ISC or GCMT (Table 2). Out of the
426 remaining 9 sequences, 7 were triggered by normal faulting GCMT events, for which we computed
427 modified Omori's law parameters (equation 2). The sequences 1, 5, 6, 8 and 10 shown in Figures
428 S8, S12, S13, S15 and S16 have p -value < 0.8 ; hence could not be classified as pure tectonic
429 mainshock-aftershock sequences (Utsu et al., 1995; Schmid and Grasso, 2012). Sequence 2 (Figure
430 S9) has a p -value > 0.8 , but was not triggered by a high-magnitude earthquake; hence not classified
431 as a typical tectonic mainshock-aftershock sequence. Although the remaining sequences 3, 4 and
432 7 shown in Figure S10, S11 and S14 were triggered by $M_w > 4.8$ events, they were not considered
433 as purely tectonic in nature as they lasted only for a few hours, a duration too short for an aftershock
434 sequence based on the statistical studies of Hainzl et al. (2016). For instance, these authors showed
435 that aftershocks for a $M_w > 4.8$ tectonic event will last for over 7 days. Sequence 11 was triggered
436 by a $m_b = 3.8$ ISC event (Figure S17), after which the number of events kept increasing instead of
437 decreasing as expected for a tectonic sequence. In short, none of the sequences in this seismic
438 swarm appeared purely tectonic in nature. The normal faulting events which triggered changes in
439 the seismic activity rate are thus interpreted as magmato-tectonic earthquakes (McNutt, 1996;
440 Rubin and Gillard, 1998; Müller and Jokat 2000). In short, the sequences triggered by strong
441 normal faulting events, were interpreted as magmato-tectonic in nature, and the others as magmatic
442 swarms. We will discuss the two remaining sequences (9 and 12) in more details further.

443 **Table 2:** Summary of number of events, tidal correlation, modified Omori's law parameters of 12

444 sequences and interpretation

| Sr No | Dates | Duration (hours) | Nbr of OHA events | Impulsive events | ISC event | GCMT event | Tidal correlation | K | c | p-value | Interpretation |
|-----------|----------------------------|------------------|-------------------|------------------|------------------------------|------------------------------|-------------------|--------------|-------------|-------------|--------------------------------------|
| 1 | 09/06/16 - 10/06/16 | 26 | 136 | 0 | N/A | N/A | NO | 23.99 | 0.01 | 0.55 | Magmatic swarm |
| 2 | 18/06/16 - 24/06/16 | 144 | 786 | 0 | N/A | N/A | NO | 179.13 | 0.09 | 0.87 | Magmatic swarm |
| 3 | 30/06/16 - 02/07/16 | 60 | 515 | 1 | $mb = 5.2$ | $Mw = 5.1$ | NO | 14.47 | 0.09 | 0.88 | Magmato-tectonic |
| 4 | 05/08/16 - 06/08/16 | 30 | 230 | 2 | $mb = 4.7$ | $Mw = 4.8$ | NO | 198.95 | 0.01 | 0.86 | Magmato-tectonic |
| 5 | 25/08/16 - 26/08/16 | 46 | 130 | 0 | $mb = 4.5$ | $Mw = 5.2$ | NO | 90.95 | 0.07 | 0.58 | Magmato-tectonic |
| 6 | 16/09/16 - 19/09/16 | 55 | 201 | 0 | $mb = 5.5$ | $Mw = 5.5$ | NO | 9.91 | 0.01 | 0.74 | Magmato-tectonic |
| 7 | 02/10/16 - 04/10/16 | 55 | 357 | 1 | $mb = 4.8$ | $Mw = 4.9$ | NO | 8.16 | 0.07 | 0.95 | Magmato-tectonic |
| 8 | 06/10/16 - 07/10/16 | 24 | 86 | 0 | $mb = 4.7$ | $Mw = 4.9$ | NO | 10.99 | 0.05 | 0.66 | Magmato-tectonic |
| 9 | 14/12/16 - 16/12/16 | 37 | 269 | 0 | N/A | N/A | YES | 14.37 | 0.01 | 0.84 | Magma upwelling |
| 10 | 26/12/16 - 27/12/16 | 29 | 124 | 0 | $mb = 3.8$ | N/A | NO | 18.34 | 0.09 | 0.57 | Magmatic swarm |
| 11 | 07/01/17 - 14/01/17 | 182 | 555 | 3 | $mb = 3.8$ | N/A | NO | 91.06 | 0.09 | 0.91 | Magmatic swarm |
| 12 | 29/01/17 - 30/01/17 | 17 | 51 | 9 | $mb = 5.7$ | $Mw = 5.4$ | NO | 62.99 | 0.07 | 0.54 | Extrusion after vertical dike |

445

446 · N/A means there was no triggering event at the start of the sequence, otherwise its magnitude is given

447 · Modified Omori's law parameters

448 · Detailed description in Figure 7 and 8

449

450 **Temporal distribution of events and tidal effects**

451 In this seismic swarm, the temporal occurrence of events displays an oscillatory pattern

452 (Figure 4b) which could be related to either ocean or solid-Earth cyclic tides (Sahoo et al., 2021).

453 Several studies have pointed out a tidal triggering of MOR seismicity (Wilcock, 2001; Scholz et

454 al., 2019), with increased seismicity at low tide (Tolstoy et al., 2002; Wilcock, 2009). To test the

455 tidal influence on the seismicity near the Melville TF, we have computed the tidal coefficients for

456 both the ocean and solid-Earth tides using a program for Global Oceanic Tidal Corrections

457 (GOTIC2; Matsumoto et al., 2001). It uses Farrell's convolution integral based on an ocean tide

458 model, a land-sea database and a mass loading Green's Function (Farrell, 1972). Near the Melville
459 TF, the ocean tide varies within ± 2 m and the solid-Earth tide within ± 40 cm. To test their
460 influence on the seismicity, we computed the number of hydroacoustic events with respect to the
461 2nd derivative of both ocean and solid-Earth tide individually. This 2nd derivative measures the
462 rate of change of slope in the tide height; thus, a negative value corresponds to high tide and a
463 positive value to low tide. In our study, 13524 events occurred during high ocean tide and 14100
464 events during low ocean tide, showing no obvious effect of the ocean tide (Figure S18). Similarly,
465 13907 and 13717 events occurred during high and low solid-Earth tides, respectively. These results
466 indicate that neither the ocean nor the solid-Earth tidal oscillations clearly govern the seismicity,
467 unlike, for instance, at Axial volcano on Juan de Fuca ridge where the seismicity was predominant
468 during the periods of low tide (Tolstoy et al., 2002; Wilcock et al., 2016).

469 We also computed the ocean and solid-Earth tidal heights for all 12 sequences and verified
470 whether there was any correlation between the tides and the seismic activity. Only for sequence 9,
471 we could observe that a high seismicity rate coincides with a high ocean tide at the start of the
472 sequence (Table 2). In order to illustrate the range of our observations, we describe two sequences
473 (9 and 12) in the next section that display very distinct characteristics.

474

475 **Geographical distribution of events**

476 At the onset of seismic activity, the hydroacoustic events had a scattered spatio-temporal
477 distribution (Figure 6), with significant fluctuations in the distance to the RP (Figure 4c). In June
478 and July 2016, events were spread over the transform valley and bathymetric highs on the southern
479 flank of the axial valley, east of the TF. One explanation could be that their seismic sources took
480 place in a wide area but it is also possible that their sources originated deep within the crust and

481 that the rough seafloor caused hydroacoustic waves to undergo propagation scattering, or wider
482 seismic/acoustic conversion area (Park et al., 2001; Williams et al., 2006). During the following
483 months, the locations of the hydroacoustic events gradually narrowed down to a stripe along the
484 ridge axis or near bathymetric highs on the flank of axial valley (Figure 4c). Although, individual
485 bursts of seismic activity clearly stand out, no clear lateral migration of the hydroacoustic events
486 could be observed during the entire period. Instead, the observed pattern over time could be
487 explained by a combination of radial focusing as well as upward migration of the seismic sources.
488 One potential geometry that would explain such observations could be diking episodes feeding
489 from magma pooling at the base of the lithosphere. The occurrence of several impulsive events
490 during this initial period (June to October, 2016) could suggest that few of the dikes emplaced on
491 the seafloor, causing lava-seawater interactions.

492 On December 14, 2016, the events clustered within a 20 x 20 km area (sequence 9 in Table
493 2 and Figure 7a) and their rate abruptly increased to ~17 events per hour (from 08:00 to 12:00),
494 followed by a gradual decrease of activity (Figure 7b). We attempted to fit a modified Omori's law
495 (Figure 7c), and obtained a *p*-value of 0.84. Although such *p*-value falls in the range of 0.8-1.2
496 associated with the tectonic mainshock-aftershock sequences (e.g., Utsu et al., 1995; Utsu, 1999;
497 Schmid and Grasso, 2012), we did not consider this sequence as purely tectonic in origin since it
498 did not feature a triggering energetic earthquake (Figure 7b). Figure 7d shows that the sudden rise
499 in the number of events occurs at oceanic high tide; however, we could not find any causality. The
500 spatial clustering of events combined with a lack of the impulsive events argue for a dike
501 emplacement that did not reach the seafloor. This scenario is illustrated by a cartoon (Figure 7e),
502 where all the hydroacoustic events from 14 to 16 December, 2016 are projected along a SW-NE
503 direction, at the apex of the potential dike.

504 After January 29, 2017, the seismicity spread in another narrow and longer band along the
505 SWIR axis (sequence 12 in Table 2 and Figure 8a). The onset of this series of events coincides
506 with a $M_w=5.4$, 12 km deep, normal faulting event on January 29-16:42 (SL = 222.5 dB), after
507 which the number of events gradually decreases as well as their SLs (inside dashed rectangle in
508 Figure 8b). Despite these characteristics, this sequence is not considered as purely tectonic
509 mainshock-aftershocks; the Omori's law p -value is only 0.54 (Figure 8c), which is much less than
510 0.8. Furthermore, the sequence only lasted for ~ 17 hours when it should have lasted at least for
511 ~ 10 days for a $M_w = 5.4$ tectonic event (Hainzl et al., 2016). Hence, this sequence is likely to have
512 a magmato-tectonic origin (Rubin, 1992; Giusti et al., 2018). Unlike the sequence in December
513 2016, tidal loading appears uncorrelated with seismicity rates (Figure 8d). We computed the stress
514 change as a result of slip along a normal fault in an elastic half-space (Meade, 2007). From the two
515 focal planes, we selected the fault plane that dips at 46° towards the axial valley (Figure 8e).
516 Assuming the hydroacoustic relocation (SE of the ridge axis) and the depth from the GCMT
517 catalog (12 km), the $M_w=5.4$ event imparted horizontal extension onto the shallow crust below
518 the axial valley, which could have triggered or facilitated the propagation of a vertical dike. The
519 narrow band of events that we interpret as a vertical and elongated dike below the axial valley, has
520 the same SW-NE azimuth as the normal fault bounding the axial valley to the south. The presence
521 of impulsive events argues for the development of a volcanic fissure along the ridge axis. Such an
522 oblique orientation with respect to the spreading direction is expected near the transform valley
523 due to a rotation of extensional stresses. Afterwards, events scattered over a wider area in
524 February-March 2017 as a result of stress-readjustment in the vicinity (Sohn et al., 1998; Dziak et
525 al., 2004; Rivalta et al., 2015). In this last stage, a double-couple event occurred in February 2017
526 with a focal mechanism parallel to the Melville TF.

527 **Succession of dike emplacements and normal faulting events**

528 Migration of seismic activity and earthquake locations has been observed at both subaerial
529 and submarine MORs and has been attributed to the vertical and/or lateral propagation of a magma-
530 filled dike at the ridge axis (e.g., Dziak *et al.* 1995; Dziak and Fox 1999; Dziak 2004; Bohnenstiehl
531 *et al.* 2004). Several laterally migrating dike intrusions have already been documented on the
532 SWIR: at segment 18 near the Novara TF and at segment 4 near the RTJ (Ingale *et al.*, 2021), and
533 at segments 7 and 8, east of the Melville TF (Schmid *et al.*, 2017). In this study, we do not observe
534 any lateral migration in the seismic activity. We interpret the bursts of seismic activity as diking
535 episodes, as evidenced by the clustering of events near bathymetric highs at 61°25'E in December
536 2016 and along a narrow band in the axial valley in January 2017. Moreover, the occurrence of
537 impulsive events suggests that magma has erupted on the seafloor, although there is so far no *in*
538 *situ* evidence for it (in the absence of recent multibeam bathymetry or side-scan sonar surveys).
539 The normal faulting GCMT and other strong earthquakes (ISC catalog) before December 2016
540 could have changed the stress regime in the sub-axial crust, changing the overpressure on a sub-
541 seafloor magma body and triggering the emplacement of several dikes (Cannat *et al.*, 2003; Baer
542 *et al.*, 2008; Standish and Sims, 2010; Liu and Buck, 2018; Olive and Dublanchet, 2020) and the
543 events after December 2016 likely represented the reactivation of faults in response to stress
544 perturbation caused after the magma eruption (Toda *et al.*, 2002; Shuler and Nettles, 2012). As
545 summarized in Table 2, we propose that these strong tectonic events occur in magmatic swarms,
546 instead of distinct mainshock-aftershock sequences, as described by McNutt (1996) in a volcanic
547 context, and have a magmato-tectonic origin as described by Rubin and Gillard (1998). Similar
548 observations of a magmatic swarm comprising several normal faulting events were made on the
549 ultraslow-spreading Gakkel ridge (Müller and Jokat 2000) and later confirmed by *in situ* sonar

550 imaging (Edwards et al., 2001). The combined evidence of seismic activity bursts, absence of clear
551 mainshock-aftershock sequences and occurrence of impulsive events point to a magmatic origin
552 for this long-lasting and intense swarm near the Melville TF.

553

554 **Conclusions**

555 Due to the remoteness of the Southwest Indian Ridge, most of its seismicity is known from
556 teleseismic records over several decades but limited to magnitudes larger than $mb = 4.5$.
557 Furthermore, *in situ* seismicity recordings with ocean bottom seismometers are rare and limited in
558 time. Long-term seismic monitoring with autonomous hydrophone networks bridges this gap by
559 capturing lower magnitude (down to $mb = 3.3$, this study) and transient events.

560 Here, we analyzed hydroacoustic T-waves associated with a swarm that occurred in 2016-
561 2017, near the Melville TF, along the SWIR, using data from the OHASISBIO and IMS-CTBTO
562 hydrophone networks. The main findings of this study are:

- 563 1. This swarm lasted for 298 days from June 01, 2016 to March 25, 2017 and counted 27624
564 hydroacoustic events, the strongest swarm reported on the SWIR so far.
- 565 2. The detection of events over two iterations reduced the uncertainties in location (latitude
566 and longitude) and origin time by ~ 8 -fold; these were improved to less than 400 m in
567 latitude and longitude and 0.1 s in origin time. Although there was a short period of noisy
568 data, the general high detection level and small location errors allow to detect individual
569 bursts of activity within this seismic swarm.
- 570 3. Although T-wave catalogs lack information about the source depth, we interpret the
571 gradual clustering of earthquakes and the different bursts of seismic activity to suggest
572 several dike emplacements. In addition, bands of events parallel to the SWIR axis imply

573 the transport of magma along narrow and elongated vertical dikes. Normal faulting events
574 were observed as magmato-tectonic in origin and associated with fault activation as well
575 as a response to stress perturbation.

576 4. We detected a series of energetic and short duration (10 -15s) impulsive events, up to ~2000
577 km away from their source. We interpret them as water-borne H-waves associated with hot
578 lava seawater interactions caused by magma emplacement on the seafloor. However, there
579 is yet no *in situ* evidence to confirm any recent eruption near the Melville TF, which calls
580 for future oceanic campaigns.

581 5. The occurrence of impulsive events, the spatio-temporal distribution of the events and the
582 absence of clear tectonic mainshock-aftershock sequences point to the magmatic nature of
583 this swarm.

584 In this study, we have visually examined and manually picked the T-wave signals to
585 understand the spatio-temporal distribution of seismicity and nature of the seismic swarm. T-wave
586 signals are more easily discernible in spectrograms than in waveforms, particularly for low-
587 magnitude events. Such analytical procedure is cumbersome and its efficiency may differ from
588 one operator to another. As a prospective, designing an algorithm based on machine-learning
589 would be a tremendous improvement (Raumer et al., 2023).

590 **Data and Resources:** Focal mechanism solutions were obtained from the GCMT catalog
591 (Ekström et al., 2012). Ocean and solid-Earth tide heights shown in this study were computed with
592 the Global Oceanic Tidal Corrections program (GOTIC2; Matsumoto et al., 2001). The
593 hydroacoustic data was analyzed with the ‘*Seas*’ software developed at the Pacific Marine
594 Environment Laboratory (PMEL; Fox et al., 2001). The detailed earthquake catalog presented in
595 this study is available upon request from the senior authors (SB & JYR). The supplementary

596 material provides plots of RLs of some representative events, of the improvements in the location
597 and time errors, of the ISC catalogue events along the SWIR from 2010 to 2020, of the impulsive
598 signal waveforms from this study and volcano off Mayotte Island, of the spatio-temporal
599 distribution as well as modified Omori's law fitting of the sequences studied, of the number of
600 hydroacoustic events with respect to tidal heights. All the figures were drafted with the Generic
601 Mapping Tool (GMT; Wessel and Smith, 1998).

602 **Acknowledgments:** The French Polar Institute (IPEV) and the French Oceanographic Fleet
603 funded the ship time for the deployment and recovery of the OHASISBIO network. INSU-CNRS
604 provided additional support and the Regional Council of Brittany (CPER) funded the hydrophone
605 moorings. V.V.I. was supported by a fellowship from the University of Brest and from the
606 Regional Council of Brittany, through the ISblue project, Interdisciplinary graduate school for the
607 blue planet (ANR-17-EURE-0015) and co-funded by a grant from the French government under
608 the program "Investissements d'Avenir" embedded in France 2030. The authors wish to thank the
609 captains and crew of RV *Marion Dufresne* for the successful deployments and recoveries of the
610 hydrophones of the OHASISBIO experiment. The authors acknowledge anonymous reviewers for
611 their insightful comments and suggestions to improve the manuscript and discussion about the
612 impulsive events.

613 **Declaration of Competing Interests:** The authors declare no competing interests.

614 **Author Contribution:** Experiment conception and data acquisition, J.Y.R.; Analysis and original
615 manuscript, V.V.I.; Manuscript edition, V.V.I., S.B. and J.Y.R.; Resources, J.Y.R. and S.B. All
616 the authors have contributed to the data interpretation and agreed to the revised version of
617 manuscript.

618 **References**

- 619 Baer, G., Y. Hamiel, G. Shamir, and R. Nof (2008). Evolution of a magma-driven earthquake
620 swarm and triggering of the nearby Oldoinyo Lengai eruption, as resolved by InSAR, ground
621 observations and elastic modeling, East African Rift, 2007, *Earth. Planet. Sci. Lett.* **272**(1-2), 0–
622 352. doi: [10.1016/j.epsl.2008.04.052](https://doi.org/10.1016/j.epsl.2008.04.052).
- 623 Baines, A. G., M. J. Cheadle, H. J. B. Dick, A. H. Scheirer, B. E. John, N. J. Kusznir, and T.
624 Matsumoto (2007), Evolution of the Southwest Indian Ridge from 55°45'E to 62°E: Changes in
625 plate-boundary geometry since 26 Ma, *Geochem. Geophys. Geosyst.* **8**, Q06022, doi:
626 [10.1029/2006GC001559](https://doi.org/10.1029/2006GC001559).
- 627 Bazin S., J.-Y., Royer, F. Dubost, F. Paquet, B. Loubrieu, A. Lavayssière, C. Deplus, N. Feuillet,
628 É. Jacques, E. Rinnert, I. Thinon, E. Lebas, D. Pierre, L. Retailleau, J.-M. Saurel, A. Sukhovich,
629 R. Bonnet and the REVOSIMA group (2022). Initial results from a hydroacoustic network to
630 monitor submarine lava flows near Mayotte Island, *C. R. Geosci.* **1**, 0, doi: [10.5802/crgeos.119](https://doi.org/10.5802/crgeos.119).
- 631 Bergman, E. A., and S. C. Solomon (1990). Earthquake swarms on the Mid-Atlantic Ridge:
632 Products of magmatism or extensional tectonics? *J. Geophys. Res.* **95**, 4943–4965, doi:
633 [10.1029/JB095iB04p04943](https://doi.org/10.1029/JB095iB04p04943).
- 634 Bohnenstiehl, D. R., M. Tolstoy, R. P. Dziak, C. G. Fox, and G. Smith (2002). Aftershock
635 sequences in the mid-ocean ridge environment: An analysis using hydroacoustic data,
636 *Tectonophysics* **354**, 49–70, doi: [10.1016/S0040-1951\(02\)00289-5](https://doi.org/10.1016/S0040-1951(02)00289-5).
- 637 Bohnenstiehl, D. R., and M. Tolstoy (2003). Comparison of teleseismically and hydroacoustically
638 derived earthquake locations along the north-central Mid-Atlantic Ridge and Equatorial East
639 Pacific Rise, *Seism. Res. Lett.* **74**, 791–802, doi: [10.1785/gssrl.74.6.791](https://doi.org/10.1785/gssrl.74.6.791).
- 640 Bohnenstiehl, D. R., M. Tolstoy, M., D. K. Smith, C. G. Fox, and R. P. Dziak (2003). Time-
641 clustering behavior of spreading-center seismicity between 15 and 35 N on the Mid-Atlantic
642 Ridge: Observations from hydroacoustic monitoring, *Phys. Earth Planet. Int.* **138**, 147–161, doi:
643 [10.1016/S0031-9201\(03\)00113-4](https://doi.org/10.1016/S0031-9201(03)00113-4).
- 644 Bohnenstiehl, D. R., R. P. Dziak, M. Tolstoy, C. G. Fox, and M. Fowler, (2004). Temporal and
645 spatial history of the 1999–2000 Endeavour Segment seismic series, Juan de Fuca Ridge,
646 *Geochem. Geophys. Geosyst.* **5**(9), Q09003, doi: [10.1029/2004GC000735](https://doi.org/10.1029/2004GC000735).
- 647 Bohnenstiehl, D. R., F. Waldhauser, and M. Tolstoy (2008). Frequency-magnitude distribution of
648 microearthquakes beneath the 9°50'N region of the East Pacific Rise, October 2003 through April
649 2004, *Geochem. Geophys. Geosyst.* **9**, Q10T03, doi: [10.1029/2008GC002128](https://doi.org/10.1029/2008GC002128).
- 650 Cannat, M., C. Rommevaux-Jestin, D. Sauter, C. Deplus, and V. Mendel (1999). Formation of the
651 axial relief at the very slow spreading Southwest Indian Ridge (49° to 69°E), *J. Geophys. Res.* **104**,
652 22825–22843, doi: [10.1029/1999JB900195](https://doi.org/10.1029/1999JB900195).

653 Cannat, M., C. Rommevaux-Jestin, and H. Fujimoto (2003). Melt supply variations to a magma
654 poor ultra slow spreading ridge (Southwest Indian Ridge 61° to 69° E), *Geochem. Geophys.*
655 *Geosyst.* **4**, 9104, doi: [10.1029/2002GC000480](https://doi.org/10.1029/2002GC000480).

656 Caplan-Auerbach, J., R. P. Dziak, J. Haxel, D. R. Bohnenstiehl, and C. Garcia (2017). Explosive
657 processes during the 2015 eruption of axial seamount, as recorded by seafloor hydrophones,
658 *Geochem. Geophys. Geosyst.* **18**, 1761–1774. doi: [10.1002/2016GC006734](https://doi.org/10.1002/2016GC006734).

659 Chadwick, W. W. Jr., K. V. Cashman, R. W. Embley, H. Matsumoto, R. P. Dziak, C. E. J. de
660 Ronde, T. K. Lau, N. D. Deardorff, S. G. Merle (2008). Direct video and hydrophone observations
661 of submarine explosive eruptions at NW Rota- 1 Volcano, Mariana Arc, *J. Geophys. Res.* **113**,
662 B08S10, doi: [10.1029/2007JB005215](https://doi.org/10.1029/2007JB005215).

663 Chu, D., and G. R. Gordon (1999). Evidence for motion between Nubia and Somalia along the
664 Southwest Indian Ridge, *Nature* **398**, 64–67, doi: [10.1038/18014](https://doi.org/10.1038/18014).

665 Crone, T. J., and D. R. Bohnenstiehl (2019). Acoustic evidence of a long-lived gas-driven
666 submarine volcanic eruption in the Bismarck Sea, *Geophys. J. Int.* **217**(1), 169–178, doi:
667 [10.1093/gji/ggy542](https://doi.org/10.1093/gji/ggy542).

668 Davis, D. S., C. Frohlich (1991). Single-link cluster analysis, synthetic earthquake catalogues, and
669 aftershock identification, *Geophys. J. Int.* **104**, 2, 289–306, doi: [10.1111/j.1365-](https://doi.org/10.1111/j.1365-246X.1991.tb02512.x)
670 [246X.1991.tb02512.x](https://doi.org/10.1111/j.1365-246X.1991.tb02512.x).

671 Debayle, E., and J.-J. L  v  que (1997). Upper mantle heterogeneities in the Indian Ocean from
672 waveform inversion, *Geophys. Res. Lett.* **24**, 245–248, doi: [10.1029/96GL03954](https://doi.org/10.1029/96GL03954).

673 Dick, H. J., J. Lin, and H. Schouten (2003). An ultraslow-spreading class of ocean ridge, *Nature*
674 **426**, 405–412, doi: [10.1038/nature02128](https://doi.org/10.1038/nature02128).

675 Dziak, R. P., C. G. Fox, and A. E. Schreiner (1995). The June–July 1993 seismo- acoustic event
676 at CoAxial segment, Juan de Fuca Ridge: evidence for a lateral dike injection, *Geophys. Res. Lett.*
677 **22**, 135–138, doi: [10.1029/94GL01857](https://doi.org/10.1029/94GL01857).

678 Dziak R. P., C. G. Fox, H. Matsumoto, and A. E. Schreiner (1997). The 1992 Cape Mendocino
679 earthquake sequence: Seismo-Acoustic analysis using fixed hydrophone arrays, *Mar. Geophys.*
680 *Res.* **19**, 137–162, doi: [10.1023/A:1004256910362](https://doi.org/10.1023/A:1004256910362).

681 Dziak R. P., and C. G. Fox (1999). The January 1998 earthquake swarm at axial volcano, Juan de
682 Fuca Ridge: hydroacoustic evidence of a seafloor volcanic activity, *Geophys. Res. Lett.* **26**, 3429–
683 3432, doi: [10.1029/1999GL002332](https://doi.org/10.1029/1999GL002332).

684 Dziak, R. P., D. K. Smith, D. R. Bohnenstiehl, C. G. Fox, D. Desbruyeres, H. Matsumoto, M.
685 Tolstoy, and D. J. Fornari (2004). Evidence of a recent magma dike intrusion at the slow spreading
686 Lucky Strike segment, Mid-Atlantic Ridge, *J. Geophys. Res.* **109**, B12102, doi:
687 [10.1029/2004JB003141](https://doi.org/10.1029/2004JB003141).

688 Dziak, R. P., D. R. Bohnenstiehl, and D. K. Smith (2012). Hydroacoustic monitoring of oceanic
689 spreading centers: Past, present, and future, *Oceanography* **25**, 116–127, doi:
690 [10.5670/oceanog.2012.10](https://doi.org/10.5670/oceanog.2012.10).

691 Dziak, R. P., D. R. Bohnenstiehl, E. T. Baker, H. Matsumoto, J. Caplan-Auerbach,
692 R. W. Embley, S. G. Merle, S. L. Walker, T.-K. Lau, and W. W. Chadwick Jr. (2015). Long-term
693 explosive degassing and debris flow activity at West Mata submarine volcano, *Geophys. Res. Lett.*
694 **42**, 1480–1487, doi: [10.1002/2014GL062603](https://doi.org/10.1002/2014GL062603).

695 Edwards, M. H., G. J. Kurras, M. Tolstoy, D. R. Bohnenstiehl, B. J. Coackley, and J. R. Cochran
696 (2001). Evidence of recent volcanic activity on the ultraslow-spreading Gakkel Ridge, *Nature* **409**,
697 808–812, doi: [10.1038/35057258](https://doi.org/10.1038/35057258).

698 Ekström, G., M. Nettles, and A. M. Dziewonski (2012). The global CMT project 2004–2010:
699 Centroid-moment tensors for 13,017 earthquakes, *Phys. Earth Planet. Inter* **200–201**, 1–9, doi:
700 [10.1016/j.pepi.2012.04.002](https://doi.org/10.1016/j.pepi.2012.04.002).

701 Farrell, W. E. (1972). Deformation of the Earth by Surface Loads, *Rev. Geophys. Space Phys.* **10**,
702 761–797, doi: [10.1029/RG010i003p00761](https://doi.org/10.1029/RG010i003p00761).

703 Forsyth, D. W., R. L. Ehrenbard, and S. Chapin (1987). Anomalous upper mantle be- neath the
704 Australian-Antarctic discordance, *Earth Planet. Sci. Lett.* **84**, 471–478, doi: [10.1016/0012-
705 821X\(87\)90011-2](https://doi.org/10.1016/0012-821X(87)90011-2).

706 Fox, C. G., R. P. Dziak, H. Matsumoto, and A. E. Schreiner (1994). Potential for monitoring low-
707 level seismicity on the Juan-de-Fuca ridge using military hydrophone arrays, *Mar. Technol. Soc.*
708 *J.* **27**, 22–30.

709 Fox, C., and V. A. Squire (1994). On the oblique reflexion and transmission of ocean waves at
710 shore fast sea ice, *Phil. Trans. R. Soc. Lond. A* **347**, 185–218, doi: [10.1098/rsta.1994.0044](https://doi.org/10.1098/rsta.1994.0044).

711 Fox, C. G., W. E. Radford, R. P. Dziak, T. K. Lau, H. Matsumoto, and A. E. Schreiner (1995).
712 Acoustic detection of a seafloor spreading episode on the Juan de Fuca Ridge using military
713 hydrophone arrays, *Geophys. Res. Lett.* **22**, 131–134, doi: [10.1029/94GL02059](https://doi.org/10.1029/94GL02059).

714 Fox, C. G., H. Matsumoto, and T. K. A. Lau (2001). Monitoring Pacific Ocean seismicity from an
715 autonomous hydrophone array, *J. Geophys. Res.* **106**, 4183–4206, doi: [10.1029/2000JB900404](https://doi.org/10.1029/2000JB900404).

716 Gibbons, S. J. (2022). The Hydroacoustic Network of the CTBT International Monitoring System:
717 Access and Exploitation, *Journal for Peace and Nuclear Disarmament*, 1–17,
718 doi: [10.1080/25751654.2022.2129948](https://doi.org/10.1080/25751654.2022.2129948).

719 Giusti, M., J. Perrot, R. P. Dziak, A. Sukhovich, and M. Maia (2018). The August 2010 earthquake
720 swarm at North FAMOUS–FAMOUS segments, Mid-Atlantic Ridge: Geophysical evidence of
721 dike intrusion, *Geophys. J. Int.* **215**, 181–195, doi: [10.1093/gji/ggy239](https://doi.org/10.1093/gji/ggy239).

- 722 Green, D. N., L. G. Evers, D. Fee, R. S. Matoza, M. Snellen, P. Smets, and D. Simons (2013).
723 Hydroacoustic, infrasonic and seismic monitoring of the submarine eruptive activity and sub-aerial
724 plume generation at South Sarigan, May 2010, *J. Volcanol. Geotherm. Res.* **257**, 31-43, doi:
725 [10.1016/j.jvolgeores.2013.03.006](https://doi.org/10.1016/j.jvolgeores.2013.03.006).
- 726 Grevemeyer, I., N. W. Hayman, D. Lange, C. Peirce, C. Papenberg, H. J. A. Van Avendonk, F.
727 Schmid, L. G. de La Peña, and A. Dannowski (2019). Constraining the maximum depth of brittle
728 deformation at slow- and ultraslow-spreading ridges using microseismicity, *Geology* **47** (11),
729 1069–1073, doi: [10.1130/G46577.1](https://doi.org/10.1130/G46577.1).
- 730 Gutenberg, B., and C. F. Richter (1954). *Seismicity of the Earth and Associated Phenomena*,
731 Princeton University Press: Princeton, NJ, USA.
- 732 Hainzl, S., A. Christophersen, D. Rhoades, and D. Harte (2016). Statistical estimation of the
733 duration of aftershock sequences, *Geophys. J. Int.* **205**(2), 1180–1189, doi: [10.1093/gji/ggw075](https://doi.org/10.1093/gji/ggw075).
- 734 Ingale V. V., S. Bazin, and J.-Y. Royer (2021). Hydroacoustic observations of two contrasted
735 seismic swarms along the Southwest Indian Ridge in 2018, *Geosciences* **11**(6), 225, doi:
736 [10.3390/geosciences11060225](https://doi.org/10.3390/geosciences11060225).
- 737 ISC International Seismological Center, On-Line Bulletin (2022), Available online:
738 <http://www.isc.ac.uk/iscbulletin/search/catalogue/> (last accessed on 10 January 2022).
- 739 Jamet, G., C. Guennou, L. Guillon, and J.-Y. Royer (2013). T-wave generation and propagation:
740 a comparison between data and spectral element modeling, *J. Acoust. Soc. Am.* **134**, 3376-3385,
741 doi: [10.1121/1.4818902](https://doi.org/10.1121/1.4818902).
- 742 Jensen, F. B., W. A. Kuperman, M. B. Porter, and H. Schmidt (1994). *Computational Ocean*
743 *Acoustic*, American Institute of Physics, New York, 14-15.
- 744 Kisslinger, C., and L. M. Jones (1991). Properties of aftershock sequences in Southern California,
745 *J. Geophys. Res.* **96**, 11947 – 11958, doi: [10.1029/91JB01200](https://doi.org/10.1029/91JB01200).
- 746 Klein, F. W., T. Wright, and J. Nakata (2006). Aftershock decay, productivity, and stress rates in
747 Hawaii: indicators of temperature and stress from magma sources, *J. geophys. Res.* **111**(B7),
748 B07307, doi: [10.1029/2005JB003949](https://doi.org/10.1029/2005JB003949).
- 749 Korger, E. I. M., and V. Schlindwein (2012). Performance of localization algorithms for
750 teleseismic mid-ocean ridge earthquakes: The 1999 Gakkel Ridge earthquake swarm and its
751 geological interpretation, *Geophys. J. Int.* **188**, 613–625, doi: [10.1111/j.1365-246X.2011.05282.x](https://doi.org/10.1111/j.1365-246X.2011.05282.x).
- 752 Läderach, C., E. I. M. Korger, V. Schlindwein, C. Müller, and A. Eskstaller (2012). Characteristics
753 of tectonomagmatic earthquake swarms at the Southwest Indian Ridge between 16°E and 25°E,
754 *Geophys. J. Int.* **190**, 429–441, doi: [10.1111/j.1365-246X.2012.05480.x](https://doi.org/10.1111/j.1365-246X.2012.05480.x).

- 755 Le Saout, M., D. R. Bohnenstiehl, J. B. Paduan, and D. A. Clague (2020). Quantification of
756 eruption dynamics on the north rift at Axial Seamount, Juan de Fuca Ridge, *Geochem. Geophys.*
757 *Geosyst.* **21**(9), e2020GC009136, doi: [10.1029/2020GC009136](https://doi.org/10.1029/2020GC009136).
- 758 Leroy, E. C., F. Samaran, J. Bonnel, and J.-Y. Royer (2017). Identification of two potential whale
759 calls in the southern Indian Ocean, and their geographic and seasonal occurrence, *J. Acoust. Soc.*
760 *Am.* **142**, 1413, doi: [10.1121/1.5001056](https://doi.org/10.1121/1.5001056).
- 761 Liu, Z., and W. R. Buck (2018). Magmatic controls on axial relief and faulting at mid-ocean ridges,
762 *Earth Planet. Sci. Lett.* **491**, 226-237, doi: [10.1016/j.epsl.2018.03.045](https://doi.org/10.1016/j.epsl.2018.03.045).
- 763 Matsumoto, K., T. Sato, T. Takanezawa, and M. Ooe (2001). GOTIC2: A Program for
764 Computation of Oceanic Tidal Loading Effect, *J. Geod. Soc. Jpn.* **47** (1), 243-248, doi:
765 [10.11366/sokuchi1954.47.243](https://doi.org/10.11366/sokuchi1954.47.243).
- 766 McNutt, S.R. (1996). Seismic Monitoring and Eruption Forecasting of Volcanoes: A Review of
767 the State-of-the-Art and Case Histories, *Monitoring and Mitigation of Volcano Hazards*. Springer,
768 Berlin, Heidelberg, doi: [10.1007/978-3-642-80087-0_3](https://doi.org/10.1007/978-3-642-80087-0_3).
- 769 McGuire J. J., M. S. Boettcher, and T. H. Jordan (2005). Foreshock sequences and short-term
770 earthquake predictability on East Pacific Rise transform faults, *Nature* **434**, 457-461, doi:
771 [10.1038/nature03377](https://doi.org/10.1038/nature03377).
- 772 Meade, B. (2007). Algorithms for the calculation of exact displacements, strains, and stresses for
773 triangular dislocation elements in a uniform elastic half space, *Comp. Geosci.* **33**(8), 1064-1075,
774 doi: [10.1016/j.cageo.2006.12.003](https://doi.org/10.1016/j.cageo.2006.12.003).
- 775 Meier, M., and V. Schlindwein (2018). First in situ seismic record of spreading events at the
776 ultraslow spreading Southwest Indian Ridge, *Geophys. Res. Lett.* **45**, 10360-10368, doi:
777 [10.1029/2018GL079928](https://doi.org/10.1029/2018GL079928).
- 778 Mendel, V., D. Sauter, L. Parson, and J. R. Vanney (1997). Segmentation and morphotectonic
779 variations along a super slow-spreading center: The Southwest Indian Ridge (57°–70°E), *Mar.*
780 *Geophys. Res.* **19**, 505–533, doi: [10.1023/A:1004232506333](https://doi.org/10.1023/A:1004232506333).
- 781 Mendel, V., D. Sauter, C. Rommevaux-Jestin, P. Patriat, F. Lefebvre, and L. M. Parson (2003).
782 Magmato-tectonic cyclicity at the ultra-slow spreading Southwest Indian Ridge: Evidence from
783 variations of axial volcanic ridge morphology and abyssal hills pattern, *Geochem. Geophys.*
784 *Geosyst.* **4**, 9102, doi: [10.1029/2002GC000417](https://doi.org/10.1029/2002GC000417).
- 785 Mogi, K. (1967). Earthquakes and fractures, *Tectonophysics* **5**, 35-55, doi: [10.1016/0040-](https://doi.org/10.1016/0040-1951(67)90043-1)
786 [1951\(67\)90043-1](https://doi.org/10.1016/0040-1951(67)90043-1).
- 787 Müller, C., and W. Jokat (2000). Seismic evidence for volcanic activity discovered in Central
788 Arctic, *Eos Trans. AGU* **81**, 265–269, doi: [10.1029/00EO00186](https://doi.org/10.1029/00EO00186).

789 Okal, E.A. (2001). T-phase Stations for the International Monitoring System of the Comprehensive
790 Nuclear-Test Ban Treaty: A Global Perspective, *Seismol. Res. Lett.* **72**(2), 186-196, doi:
791 [10.1785/gssrl.72.2.186](https://doi.org/10.1785/gssrl.72.2.186).

792 Olive, J.-A., and J. Escartín (2016). Dependence of seismic coupling on normal fault style along
793 the Northern Mid-Atlantic Ridge, *Geochem. Geophys. Geosyst.* **17**, 4128-4152,
794 doi:[10.1002/2016GC006460](https://doi.org/10.1002/2016GC006460).

795 Olive, J.-A., and P. Dublanchet (2020). Controls on the magmatic fraction of extension at mid-
796 ocean ridges, *Earth Planet. Sci. Lett.* **549**, 116541, doi: [10.1016/j.epsl.2020.116541](https://doi.org/10.1016/j.epsl.2020.116541).

797 Orsi, A. H., Whitworth III, T., & Nowlin Jr, W. D. (1995). On the meridional extent and fronts of
798 the Antarctic Circumpolar Current, *Deep Sea Research Part I: Oceanographic Research Papers*
799 **42** (5), 641-673, doi: [10.1016/0967-0637\(95\)00021-W](https://doi.org/10.1016/0967-0637(95)00021-W).

800 Park, M., R. I. Odom, D. J. Soukup (2001). Modal scattering: a key to understanding oceanic T-
801 waves, *Geophys. Res. Lett.* **28** (17), 3401-3404, doi: [10.1029/2001GL013472](https://doi.org/10.1029/2001GL013472).

802 Parnell-Turner, R., D. K. Smith, and R. P. Dziak (2022). Hydroacoustic monitoring of seafloor
803 spreading and transform faulting in the equatorial Atlantic Ocean, *J. Geophys. Res. Solid Earth*
804 **127**, e2022JB024008, doi: [10.1029/2022JB024008](https://doi.org/10.1029/2022JB024008).

805 Parson, L., D. Sauter, V. Mendel, P. Patriat, and R. Searle (1997). Evolution of the Axial Geometry
806 of the Southwest Indian Ocean Ridge between the Melville Fracture Zone and the Indian Ocean
807 Triple Junction – Implications for Segmentation on Very Slow-Spreading Ridges, *Marine*
808 *Geophysical Researches* **19**, 535–552, doi: [10.1023/A:1004335919592](https://doi.org/10.1023/A:1004335919592).

809 Patriat, P., and J. Ségoufin (1988). Reconstruction of the central Indian Ocean, *Tectonophysics*
810 **155**, 211–234, doi: [10.1016/0040-1951\(88\)90267-3](https://doi.org/10.1016/0040-1951(88)90267-3).

811 Patriat, P., D. Sauter, M. Munsch, and L. M. Parson (1997). A survey of the Southwest Indian
812 Ridge axis between Atlantis II Fracture Zone and the Indian Triple Junction: Regional setting and
813 large scale segmentation, *Mar. Geophys. Res.* **19**, 457–480, doi: [10.1023/A:1004312623534](https://doi.org/10.1023/A:1004312623534).

814 Raumer P.-Y., S. Bazin, D. Cazau, J.-Y. Royer, V. V. Ingale, and A. Lavayssiere (2023).
815 Application of machine learning to hydro-acoustic seismic and magmatic events detections, EGU
816 General Assembly 2023, Vienna, Austria. Available online:
817 <https://meetingorganizer.copernicus.org/EGU23/EGU23-7028.html>.

818 Rintoul, S. R., C. Hughes, and D. Olbers (2001). The Antractic Circumpolar Current System,
819 *Ocean Circulation and Climate*. New York: Academic Press, hdl: [10013/epic.13233](https://hdl.handle.net/10013/epic.13233), ISBN: [0-12-
820 641351-7](https://doi.org/10.1016/0-12-641351-7).

821 Rivalta, E., B. Taisne, A. P. Bungler, and R. F. Katz (2015). A review of mechanical models of
822 dike propagation: Schools of thought, results and future directions, *Tectonophysics* **638**, 1–42, doi:
823 [10.1016/j.tecto.2014.10.003](https://doi.org/10.1016/j.tecto.2014.10.003).

- 824 Rommevaux-Jestin, C., C. Deplus, and P. Patriat (1997). Mantle Bouguer Anomaly Along an Ultra
825 Slow-Spreading Ridge: Implications for Accretionary Processes and Comparison with Results
826 from Central Mid-Atlantic Ridge, *Mar. Geophys. Res.* **19**, 481–503, doi:
827 [10.1023/A:1004269003009](https://doi.org/10.1023/A:1004269003009).
- 828 Royer, J.-Y., P. Patriat, H. W. Bergh, and C. R. Scotese (1988). Evolution of the Southwest Indian
829 Ridge from the Late Cretaceous (anomaly 34) to the Middle Eocene (anomaly 20), *Tectonophysics*
830 **155**, 235–260, doi: [10.1016/0040-1951\(88\)90268-5](https://doi.org/10.1016/0040-1951(88)90268-5).
- 831 Royer, J.-Y., J. G. Sclater, and D. T. Sandwell (1989). A preliminary tectonic fabric chart of the
832 Indian Ocean, *Proc. Indian Acad. Sci. Earth Planet. Sci.* **98**, 7–24, doi: [10.1007/BF02880373](https://doi.org/10.1007/BF02880373).
- 833 Royer, J.-Y. (2009). OHA-SIS-BIO: Hydroacoustic Observatory of the Seismicity and
834 Biodiversity in the Indian Ocean, Available online: <https://campagnes.flotteoceanographique.fr/>
835 (accessed on 10 January 2022).
- 836 Royer, J.-Y., R. Chateau, R. P. Dziak, and D. R. Bohnenstiehl (2015). Seafloor seismicity,
837 Antarctic ice-sounds, cetacean vocalizations and long-term ambient sound in the Indian Ocean
838 basin, *Geophys. J. Int.* **202**, 748–762, doi: [10.1093/gji/ggv178](https://doi.org/10.1093/gji/ggv178).
- 839 Rubin, A. M. (1992). Dike-induced faulting and graben subsidence in volcanic rift zones, *J.*
840 *geophys. Res.* **97**, 1839–1858, doi: [10.1029/91JB02170](https://doi.org/10.1029/91JB02170).
- 841 Rubin, A. M., and D. Gillard (1998). Dike-induced earthquakes: Theoretical considerations, *J.*
842 *Geophys. Res.* **103**(B5), 10,017–10,030, doi: [10.1029/97JB03514](https://doi.org/10.1029/97JB03514).
- 843 Rundquist, D. V., and P. O. Sobolev (2002). Seismicity of mid-oceanic ridges and its geodynamic
844 implications: A review, *Earth Sci. Rev.* **58**, 143–161, doi: [10.1016/S0012-8252\(01\)00086-1](https://doi.org/10.1016/S0012-8252(01)00086-1).
- 845 Sahoo, S., B. Senapati, D. Panda, D. K. Tiwari, M. Santosh, B. Kundu (2021). Tidal triggering of
846 micro-seismicity associated with caldera dynamics in the Juan de Fuca ridge, *J. Volcanol.*
847 *Geotherm. Res* **417**, 107319, doi: [10.1016/j.jvolgeores.2021.107319](https://doi.org/10.1016/j.jvolgeores.2021.107319).
- 848 Samaran, F., K. M. Stafford, T. A. Branch, J. Gedamke, J.-Y. Royer, R. P. Dziak, and C. Guinet
849 (2013). Seasonal and geographic variation of southern blue whale subspecies in the Indian Ocean,
850 *PLoS ONE* **8**, e71561, doi: [10.1371/journal.pone.0071561](https://doi.org/10.1371/journal.pone.0071561).
- 851 Saurel, J.-M., L. Retailleau, C. Deplus, B. Loubrieu, D. Pierre, M. Frangieh, N. Khelifi, R. Bonnet,
852 V. Ferrazzini, S. Bazin, P. Guyavarch, M. Moulin, REVOSIMA Seismology group, REVOSIMA
853 Bathymetry group (2022). Combining hydro-acoustic sources and bathymetric differences to track
854 the vent evolution of the Mayotte eruption, Mozambique Channel, *Front. Earth Sci.* 10:983051,
855 doi:[10.3389/feart.2022.983051](https://doi.org/10.3389/feart.2022.983051).
- 856 Sauter, D., V. Mendel, C. Rommevaux-Jestin, L. M. Parson, H. Fujimoto, C. Mével, M. Cannat,
857 and K. Tamaki (2004). Focused magmatism versus amagmatic spreading along the ultra-slow

858 spreading Southwest Indian Ridge: Evidence from TOBI side scan sonar imagery, *Geochem.*
859 *Geophys. Geosyst.* **5** (Q10K09), doi: [10.1029/2004GC000738](https://doi.org/10.1029/2004GC000738).

860 Sauter, D., and M. Cannat (2010). The ultraslow spreading Southwest Indian ridge, In *Diversity of*
861 *Hydrothermal Systems on Slow Spreading Ocean Ridges*; Geophysical Monograph Series; The
862 American Geophysical Union: Washington, DC, USA **188**, 153–173, doi:
863 [10.1029/2008GM000843](https://doi.org/10.1029/2008GM000843).

864 Schlindwein, V. (2012). Teleseismic earthquake swarms at ultraslow spreading ridges: indicator
865 for dyke intrusions?, *Geophys. J. Int.* **190**(1), 442–456, doi: [10.1111/j.1365-246X.2012.05502.x](https://doi.org/10.1111/j.1365-246X.2012.05502.x).

866 Schlindwein, V. and C. Riedel (2010). Location and source mechanism of sound signals at Gakkel
867 ridge, Arctic Ocean: Submarine Strombolian activity in the 1999–2001 volcanic episode,
868 *Geochem. Geophys. Geosyst.* **11**(1), doi: [10.1029/2009GC002706](https://doi.org/10.1029/2009GC002706).

869 Schlindwein, V., A. Demuth, E. Korger, C. Läderach, and F. Schmid (2015). Seismicity of the
870 Arctic mid-ocean ridge system, *Polar Sci.* **9**, 146–157, doi: [10.1016/j.polar.2014.10.001](https://doi.org/10.1016/j.polar.2014.10.001).

871 Schlindwein, V., and F. Schmid (2016). Mid-ocean-ridge seismicity reveals extreme types of
872 ocean lithosphere, *Nature* **535**, 276–279, doi: [10.1038/nature18277](https://doi.org/10.1038/nature18277).

873 Schmid, A., and J. R. Grasso (2012). Omori law for eruption foreshocks and aftershocks, *J.*
874 *Geophys. Res. Solid Earth* **117**(B7), doi: [10.1029/2011JB008975](https://doi.org/10.1029/2011JB008975).

875 Schmid, F., V. Schlindwein, I. Koulakov, A. Plötz, and J. R. Scholz (2017). Magma plumbing
876 system and seismicity of an active mid-ocean ridge volcano, *Sci. Rep.* **7**, 42949, doi:
877 [10.1038/srep42949](https://doi.org/10.1038/srep42949).

878 Schreiner, A.E., C. G. Fox, and R. P. Dziak (1995). Spectra and magnitudes of T-waves from the
879 1993 earthquake swarm on the Juan de Fuca Ridge, *Geophys. Res. Lett.* **22**, 139–142, doi:
880 [10.1029/94GL01912](https://doi.org/10.1029/94GL01912).

881 Scholz, C. H., Y. J. Tan, and F. Albino (2019). The mechanism of tidal triggering of earthquakes
882 at mid-ocean ridges, *Nat Commun.* **10**, 2526, doi: [10.1038/s41467-019-10605-2](https://doi.org/10.1038/s41467-019-10605-2).

883 Shuler, A., and M. Nettles (2012). Earthquake source parameters for the 2010 western Gulf of
884 Aden rifting episode, *Geophys. J. Int.* **190**, 111–1122, doi: [10.1111/j.1365-246X.2012.05529.x](https://doi.org/10.1111/j.1365-246X.2012.05529.x).

885 Slack, P. D., C. G. Fox, and R. P. Dziak (1999). P wave detection thresholds, Pn velocity estimates,
886 and T wave location uncertainty from oceanic hydrophones, *J. Geophys. Res.* **104**, 13061–13072,
887 doi: [10.1029/1999JB900112](https://doi.org/10.1029/1999JB900112).

888 Smith D. K., M. Tolstoy, C. G., Fox, D. R. Bohnenstiehl, H. Matsumoto, M. J. Fowler (2002).
889 Hydroacoustic monitoring of seismicity at the slow-spreading Mid-Atlantic Ridge, *Geophys. Res.*
890 *Lett.* **29** (11), doi: [10.1029/2001GL013912](https://doi.org/10.1029/2001GL013912).

891 Smith, D. K., J. Escartin, M. Cannat, M. Tolstoy, C. G. Fox, D. R. Bohnenstiehl and S. Bazin
892 (2003). Spatial and temporal distribution of seismicity along the northern Mid-Atlantic Ridge
893 (15°–35°N), *J. Geophys. Res.* **108**, 2167, doi: [10.1029/2002JB001964](https://doi.org/10.1029/2002JB001964).

894 Sohn, R. A., J. A. Hildebrand, and S. C. Webb (1998). Postdrifting seismicity and a model for the
895 1993 diking event on the CoAxial segment, Juan de Fuca Ridge, *J. Geophys. Res.* **103**, 9867–9877,
896 doi: [10.1029/98JB00391](https://doi.org/10.1029/98JB00391).

897 Standish, J. J., K. W. Sims (2010). Young off-axis volcanism along the ultraslow-spreading
898 Southwest Indian Ridge, *Nat. Geosci.* **3**, 286–292, doi: [10.1038/ngeo824](https://doi.org/10.1038/ngeo824).

899 Sykes, L. R. (1970). Earthquake swarms and sea-floor spreading, *J. Geophys. Res.* **75**
900 (32), 6598–6611, doi: [10.1029/JB075i032p06598](https://doi.org/10.1029/JB075i032p06598).

901 Tan, Y. J., M. Tolstoy, F. Waldhauser, and W. Wilcock (2016). Dynamics of a seafloor-spreading
902 episode at the east pacific rise, *Nature* **540**, 261–265, doi: [10.1038/nature20116](https://doi.org/10.1038/nature20116).

903 Teague, W. J., M. J. Carron, and J. P. Hogan (1990). A comparison between the Generalized
904 Digital Environment Model and Levitus climatologies, *J. Geophys. Res.* **95**, 7167–7183, doi:
905 [10.1029/JC095iC05p07167](https://doi.org/10.1029/JC095iC05p07167).

906 Tepp, G., and R. P. Dziak (2021). The seismo-acoustics of submarine volcanic eruptions, *J.*
907 *Geophys. Res. Solid Earth* **126**, e2020JB020912, doi: [10.1029/2020JB020912](https://doi.org/10.1029/2020JB020912).

908 Tepp, G., W. W. Chadwick Jr, M. M. Haney, J. J. Lyons, R. P. Dziak, S. G. Merle, D. A.
909 Butterfield, and C. W. Young III (2019). Hydroacoustic, seismic, and bathymetric observations of
910 the 2014 submarine eruption at Ahyi Seamount, Mariana Arc. *Geochem. Geophys. Geosyst.* **20**,
911 3608–3627, doi: [10.1029/2019GC008311](https://doi.org/10.1029/2019GC008311).

912 Tepp, G., R. P. Dziak, M. M. Haney, J. J. Lyons, C. Searcy, H. Matsumoto, and J. Haxel (2020).
913 Seismic and hydroacoustic observations of the 2016–17 Bogoslof eruption, *Bull. Volcanol.* **82**, 4,
914 doi: [10.1007/s00445-019-1344-3](https://doi.org/10.1007/s00445-019-1344-3).

915 Toda, S., R. S. Stein, and T. Sagiya (2002). Evidence from the AD 2000 Izu islands earthquake
916 swarm that stressing rate governs seismicity, *Nature* **419**, 58–61, doi: [10.1038/nature00997](https://doi.org/10.1038/nature00997).

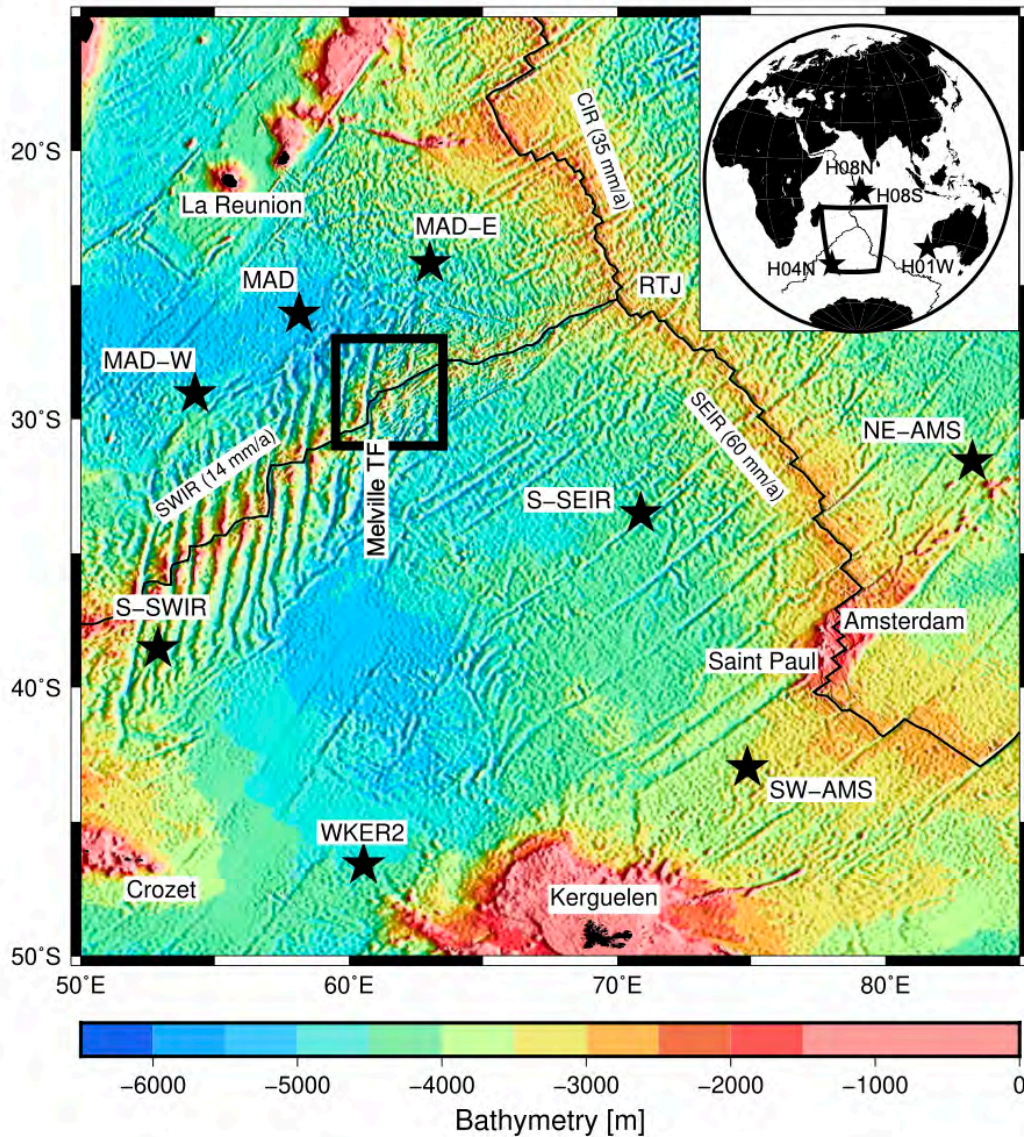
917 Tolstoy, I., and M. Ewing (1950). The T phase of shallow-focus earthquakes, *Bull. Seism. Soc.*
918 *Am.* **40**, 25–51, doi: [10.1785/BSSA0400010025](https://doi.org/10.1785/BSSA0400010025).

919 Tolstoy, M., D. R. Bohnenstiehl, M. H. Edwards, and G. J. Kurras (2001). Seismic character of
920 volcanic activity at the ultraslow-spreading Gakkel Ridge, *Geology* **29**, 1139–1142, doi:
921 [10.1130/0091-7613\(2001\)029<1139:SCOVAA>2.0.CO;2](https://doi.org/10.1130/0091-7613(2001)029<1139:SCOVAA>2.0.CO;2).

922 Tolstoy, M., F. L. Vernon, O. A. John, and W. K. (2002). Breathing of the seafloor: Tidal
923 correlations of seismicity at Axial volcano, *Geology* **30** (6), 503–506. doi: [10.1130/0091-
924 7613\(2002\)030<0503:BOTSTC>2.0.CO;2](https://doi.org/10.1130/0091-7613(2002)030<0503:BOTSTC>2.0.CO;2).

- 925 Tolstoy, M., and D. R. Bohnenstiehl (2006). Hydroacoustic contributions to understanding the
926 December 26th 2004 great Sumatra-Andaman Earthquake, *Surv. Geophys.* **27**, 633-646, doi:
927 [10.1007/s10712-006-9003-6](https://doi.org/10.1007/s10712-006-9003-6).
- 928 Tolstoy, M., F. Waldhauser, D. R. Bohnenstiehl, R. T. Weekly, and W-Y. Kim (2008). Seismic
929 identification of along-axis hydrothermal flow on the East Pacific Rise, *Nature* **451**, 181–184, doi:
930 [10.1038/nature06424](https://doi.org/10.1038/nature06424).
- 931 Toomey, D. R., S. C. Solomon, G. M. Purdy, and M. H. Murray (1985). Microearthquakes beneath
932 the median valley of the Mid-Atlantic Ridge near 23°N: Hypocenters and focal mechanisms, *J.*
933 *Geophys. Res.* **90**, 5443–5458, doi: [10.1029/JB090iB07p05443](https://doi.org/10.1029/JB090iB07p05443).
- 934 Tsang-Hin-Sun, E., J.-Y. Royer, and J. Perrot (2016). Seismicity and active accretion processes at
935 the ultraslow-spreading Southwest and intermediate-spreading Southeast Indian ridges from
936 hydroacoustic data, *Geophys. J. Int.* **206**, 1232–1245, doi: [10.1093/gji/ggw201](https://doi.org/10.1093/gji/ggw201).
- 937 Utsu, T., Y. Ogata, and R. S. Matsuura (1995). The centenary of the Omori formula for a decay
938 law of aftershock activity, *J. Phys. Earth* **1995**, 43, 1–33, doi: [10.4294/jpe1952.43.1](https://doi.org/10.4294/jpe1952.43.1).
- 939 Utsu, T. (1999). Representation and analysis of the earthquake size distribution: A historical
940 review and some new approaches, *Pure Appl. Geophys.* **155**(2–4), 509–535, doi:
941 [10.1007/s000240050276](https://doi.org/10.1007/s000240050276).
- 942 Wessel, P., and W. H. Smith (1998). New, improved version of Generic Mapping Tools released,
943 *Eos Trans. Am. Geophys. Union* **79**, 579, doi: [10.1029/98EO00426](https://doi.org/10.1029/98EO00426).
- 944 Weston, D. E., and P. B. Rowlands (1979). Guided acoustic waves in the ocean, *Rep. Prog. Phys.*
945 **42**, 347, doi: [10.1088/0034-4885/42/2/003/meta](https://doi.org/10.1088/0034-4885/42/2/003/meta).
- 946 Wiens, D. A., and D. E. Petroy (1990). The largest recorded earthquake swarm: Intraplate faulting
947 near the Southwest Indian Ridge, *J. Geophys. Res.* **95**, 4735–4750, doi:
948 [10.1029/JB095iB04p04735](https://doi.org/10.1029/JB095iB04p04735).
- 949 Wilcock, W. S. (2001). Tidal triggering of microearthquakes on the Juan de Fuca Ridge, *Geophys.*
950 *Res. Lett.* **28**(20), 3999-4002, doi: [10.1029/2001GL013370](https://doi.org/10.1029/2001GL013370).
- 951 Wilcock, W. S. (2009). Tidal triggering of earthquakes in the Northeast Pacific Ocean, *Geophys.*
952 *J. Int.* **179**(2), 1, doi: [10.1111/j.1365-246X.2009.04319.x](https://doi.org/10.1111/j.1365-246X.2009.04319.x).
- 953 Williams, C. M., R. A. Stephen, and D. K. Smith (2006). Hydroacoustic events located at the
954 intersection of the Atlantis (30°N) and Kane (23°40'N) Transform Faults with the Mid-Atlantic
955 Ridge, *Geochem. Geophys. Geosyst.* **7**, Q06015, doi: [10.1029/2005GC001127](https://doi.org/10.1029/2005GC001127).
- 956 Wolfe, C. J., G. M. Purdy, D. R. Toomey, and S. C. Solomon (1995). Microearthquake
957 characteristics and crustal velocity structure at 29°N on the Mid-Atlantic Ridge: The architecture
958 of a slow spreading segment, *J. Geophys. Res.* **100**, 24449–24472, doi: [10.1029/95JB02399](https://doi.org/10.1029/95JB02399).

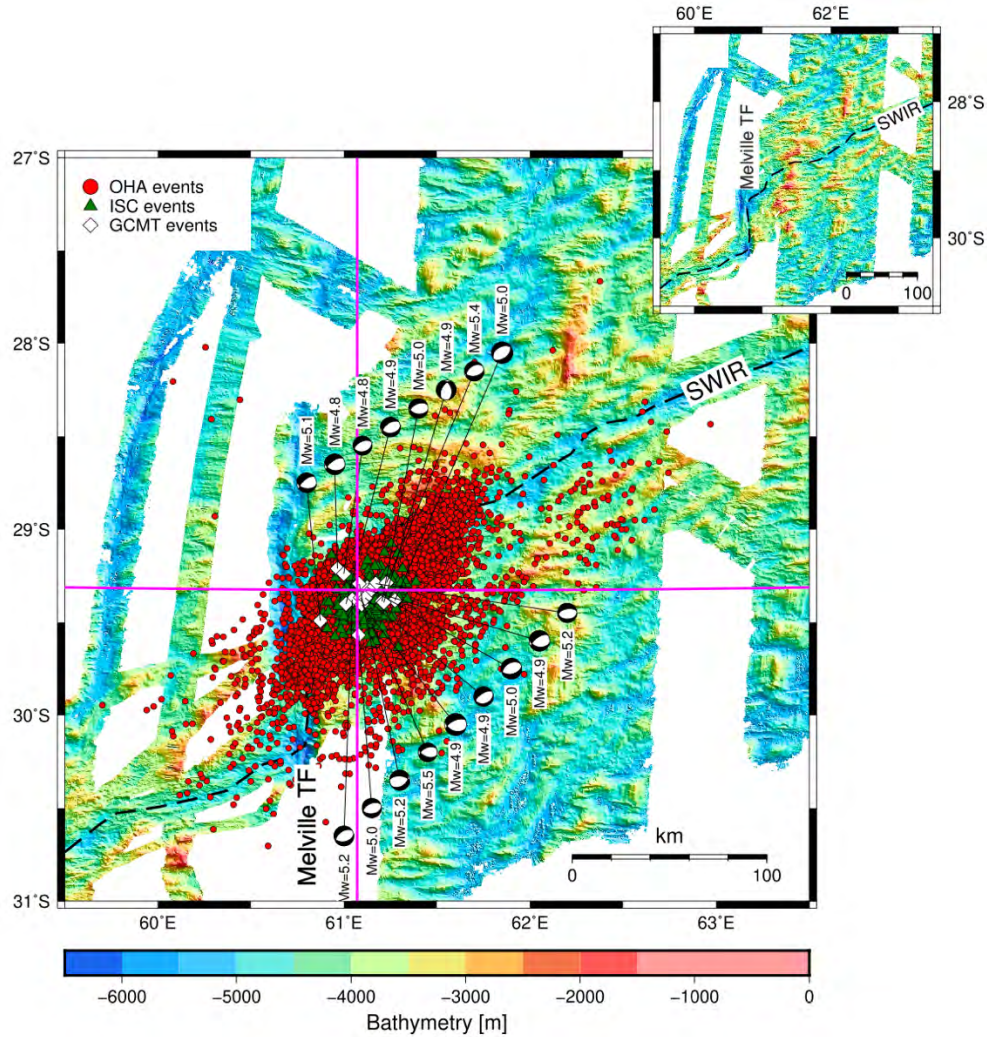
- 959 Yang, Y., and D. W. Forsyth (2003). Improving epicentral and magnitude estimation of
960 earthquakes from T phases by considering the excitation function, *Bull. Seismo. Soc. Am.* **93**(5),
961 2106 - 2122, doi: [10.1785/0120020215](https://doi.org/10.1785/0120020215).
- 962 Yu, Z., J. Li, X. Niu, N. Rawlinson, A. Ruan, W. Wang, H. Hu, X. Wei, J. Zhang, and Y. Liang
963 (2018). Lithospheric structure and tectonic processes constrained by microearthquake activity at
964 the central ultraslow-spreading Southwest Indian Ridge (49.2° to 50.8°E), *J. Geophys. Res. Solid*
965 *Earth* **123**, 6247–6262, doi: [10.1029/2017JB015367](https://doi.org/10.1029/2017JB015367).
- 966 Yu, Z., S. C. Singh, E. P. Gregory, M. Maia, Z. Wang, and D. Brunelli (2021). Semibrittle seismic
967 deformation in high-temperature mantle mylonite shear zone along the Romanche transform
968 fault, *Sci. Adv.* **7** (15), eabf3388, doi: [10.1126/sciadv.abf3388](https://doi.org/10.1126/sciadv.abf3388).



969

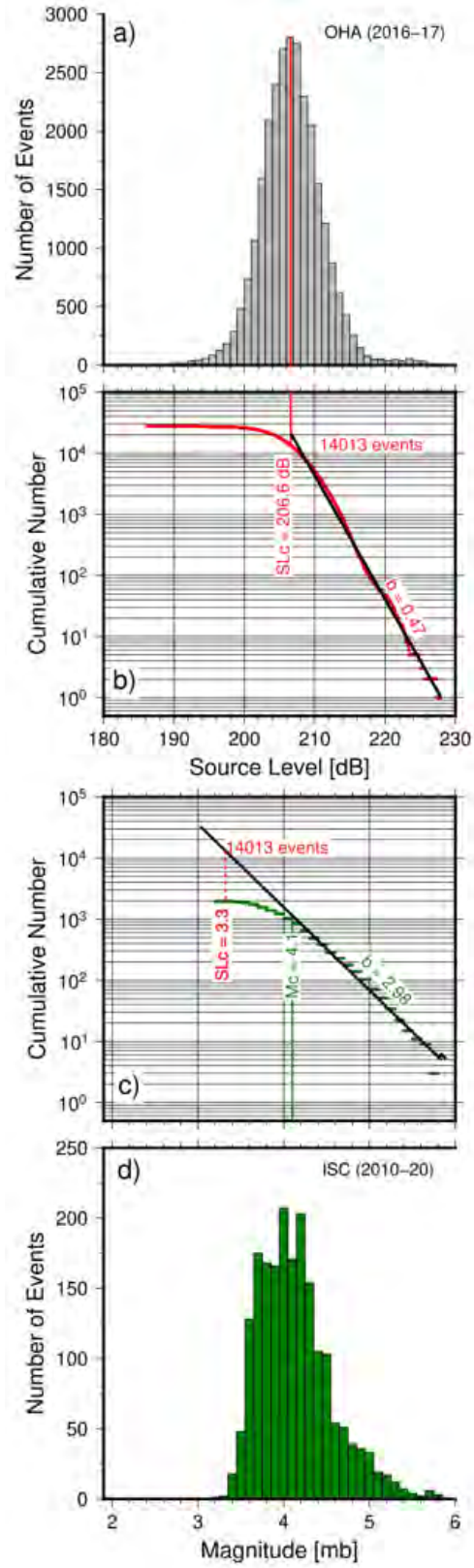
970 **Figure 1 – Bathymetric map of the southern Indian Ocean with location of the hydroacoustic**
 971 **networks:** The autonomous underwater hydrophones of the OHASISBIO and IMS-CTBTO
 972 (inset) networks are shown by stars. Black square outlines the study area around Melville TF. The
 973 TF is along the ridge axis. Black lines mark three Indian mid-oceanic ridges; the ultraslow-
 974 spreading Southwest Indian Ridge (SWIR), the slow-spreading Central Indian Ridge (CIR) and
 975 the intermediate-spreading Southeast Indian Ridge (SEIR) with their respective average spreading
 976 rates in the map region.

977

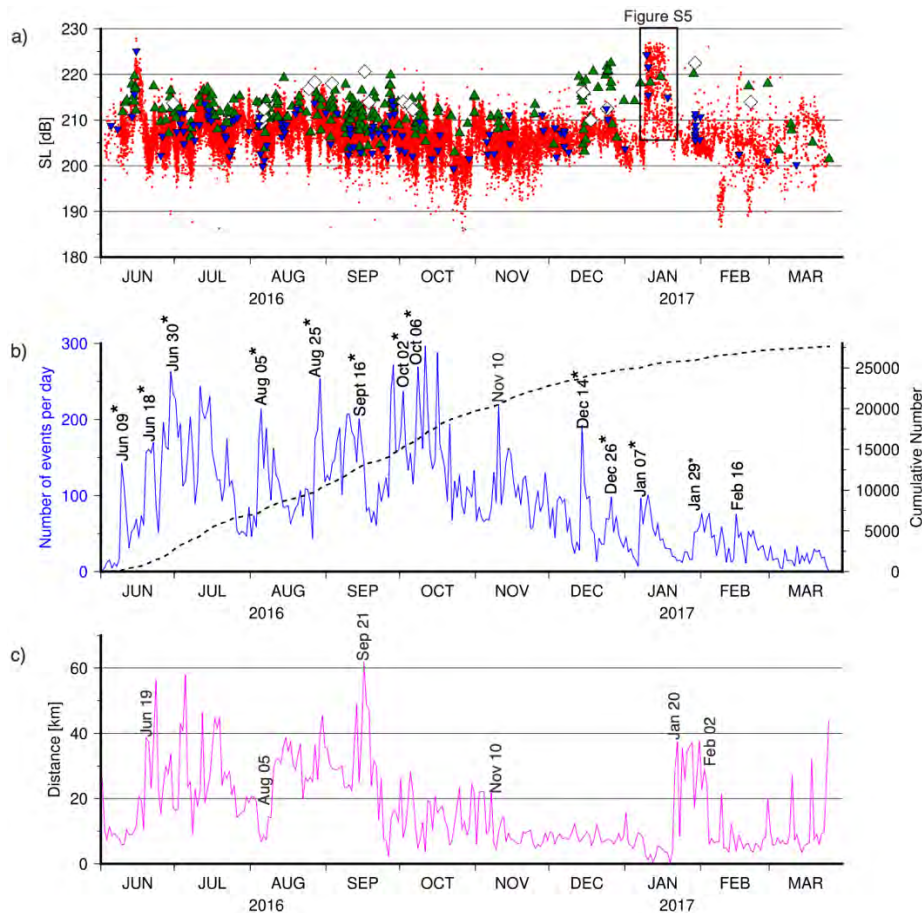


978

979 **Figure 2 - Events of the 2016-2017 seismic swarm near Melville transform fault:**
 980 Hydroacoustic events detected by the OHASISBIO network (circles), hydroacoustic locations of
 981 land-based ISC catalog (triangles) and GCMT catalog (diamonds) along with their focal
 982 mechanisms and magnitudes. The azimuths of all focal mechanisms are parallel to the SWIR axis
 983 (dashed line), except one parallel to the Melville TF. The cross is the coordinate of median location
 984 of all the detected events (hereafter called RP for reference point). Inset shows the same
 985 bathymetry map without the location of events.



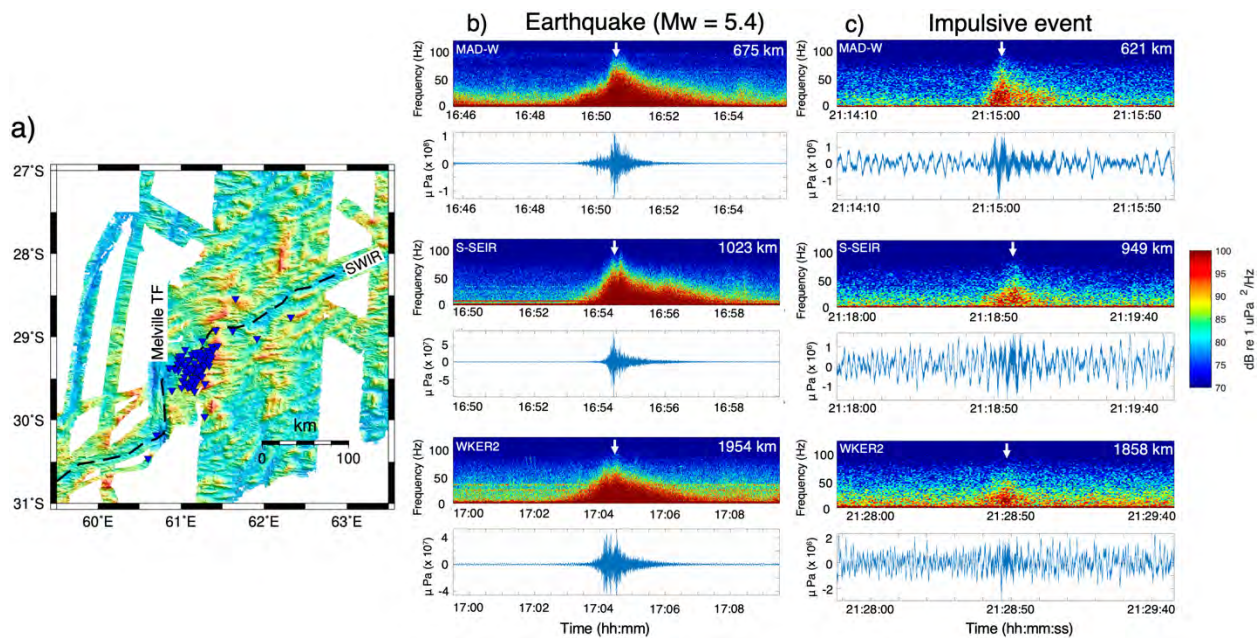
987 **Figure 3 - Source level distribution and completeness of the hydroacoustic catalog:** The
 988 completeness of SL and mb is based on the best-fitting Gutenberg-Richter lines. **a)** Histogram of
 989 the hydroacoustic events detected from June 2016 to March 2017 (OHA catalog). **b)** Cumulative
 990 number of events in the OHA catalog. The vertical line points to the completeness value, $SL_c =$
 991 206.6 dB for the OHA catalog. The b-value is estimated from the slope of 0.47 in the SL
 992 framework. **c)** Cumulative number of events in the ISC catalog reported along the SWIR axis
 993 from 2010 to 2020. The vertical line points to magnitude of completeness of the ISC catalog, $M_{c(ISC)}$
 994 = 4.1. Extrapolating the Gutenberg-Richter relationship of ISC catalog (having $b = 2.98$) upto the
 995 number of events for which OHA catalog is complete (14013 events at $SL_c = 206.6$ dB) yields a
 996 level of $M_{c(OHA)} = 3.3$ mb. **d)** Histogram of magnitudes of the ISC events along the SWIR axis.
 997



998

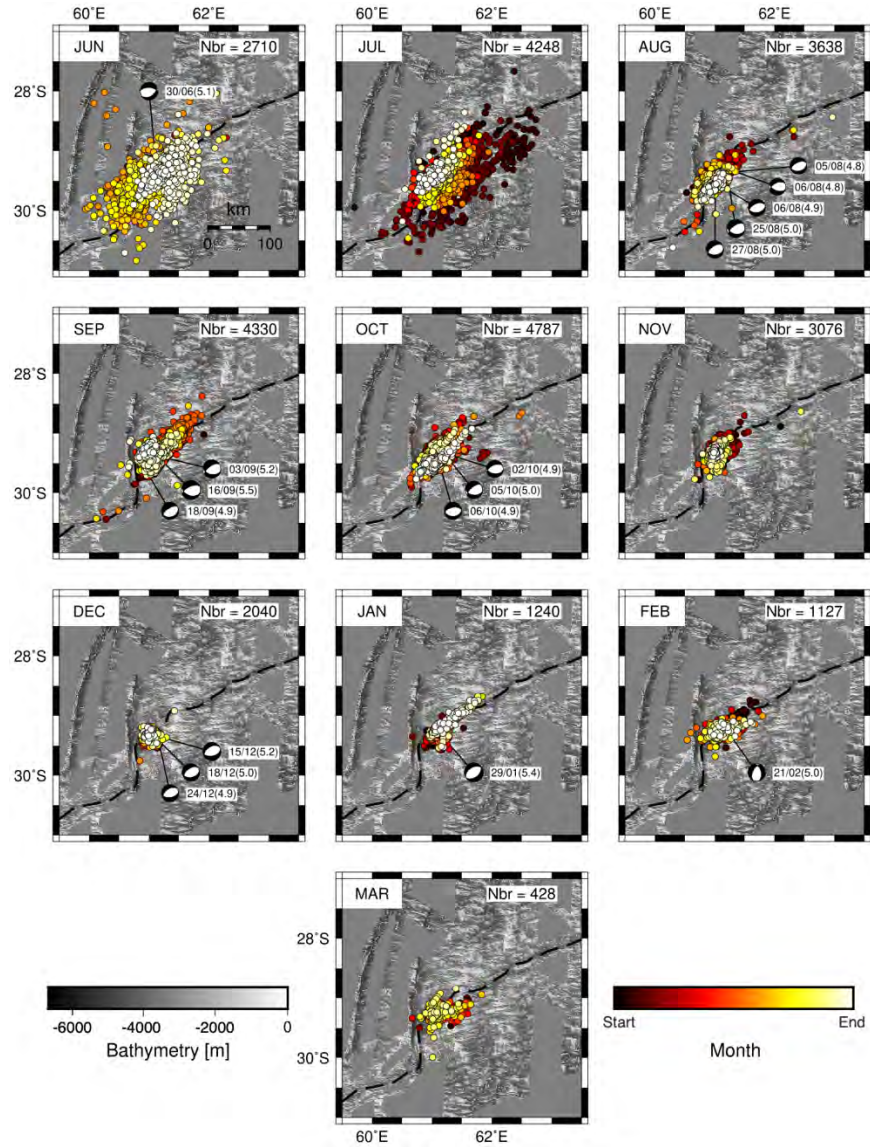
999 **Figure 4 - Temporal distribution of events:** **a)** Source Level distribution of all the hydroacoustic
 1000 events (dots), and those corresponding to the ISC (triangles), GCMT (diamonds) catalogs and

1001 impulsive events (inverted triangles) between June 2016 and March 2017. Explanation for
 1002 anomalous higher SLs of events between January 09 and January 20, 2017 (black rectangle) is
 1003 extended in Figure S5. **b**) Number of events per day (solid line) and cumulative number of
 1004 events vs. time (dashed line). The dates mark the time of higher activity rate between June 2016
 1005 and March 2017. The dates with asterisk are potential sequences to compute modified Omori's
 1006 law. **c**) Median distance of events per day relative to a reference point (RP; marked by a cross in
 1007 Figure 2). The dates mark the significant changes in the distance of events from the RP.



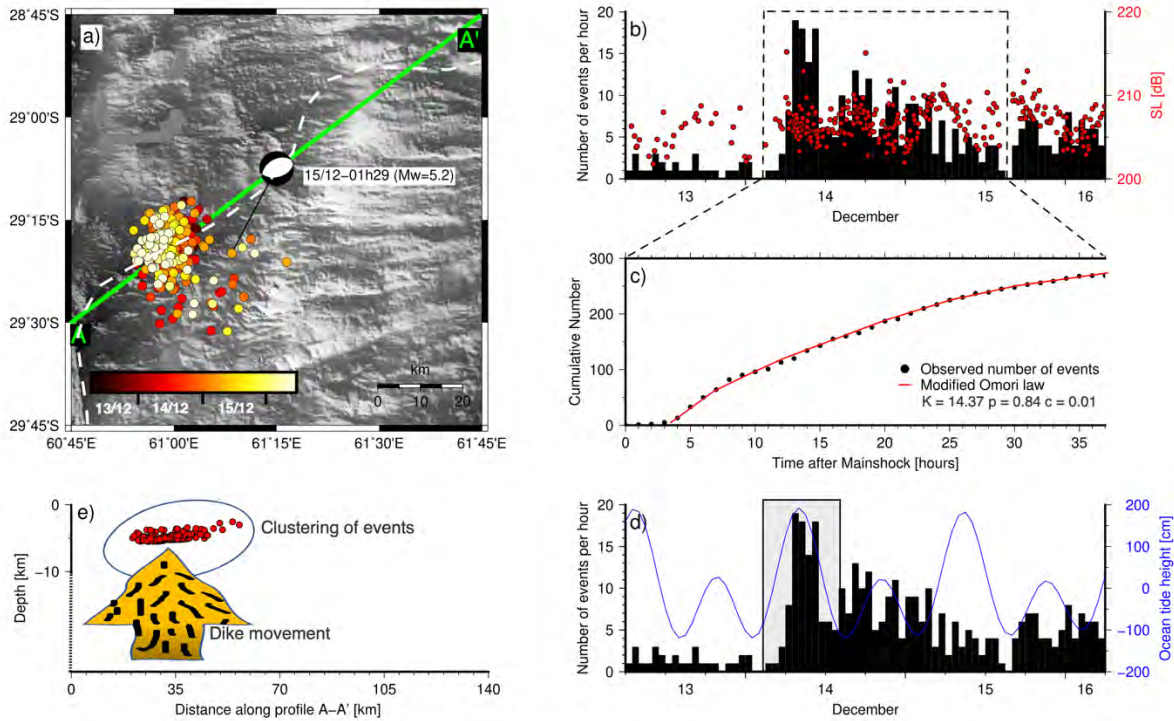
1008

1009 **Figure 5 - Impulsive events:** **a**) Impulsive events (blue triangles) are located on the slopes of
 1010 bathymetric highs, on the southern flank of the SWIR east of Melville TF. The dashed line shows
 1011 the SWIR axis. **b and c**) 10 and 2-minute-long acoustic waveforms and corresponding
 1012 spectrograms of a typical earthquake event ($M_w = 5.4$) on left and an impulsive event on right on
 1013 three hydrophones of the OHASISBIO network (MAD-W, S-SEIR, WKER2, from top to bottom)
 1014 with distances in kilometers from an earthquake in **b**) and the cluster of impulsive events in **c**). An
 1015 earthquake signal (T-wave) can last for ~ 200 s vs ~ 10 -15s for an impulsive event (H-wave).
 1016 Earthquake signals are observed both in waveform and spectrogram; however, impulsive signals
 1017 clearly stand out in spectrograms. White arrows point to the highest T-wave or H-wave energy
 1018 arrivals.



1019

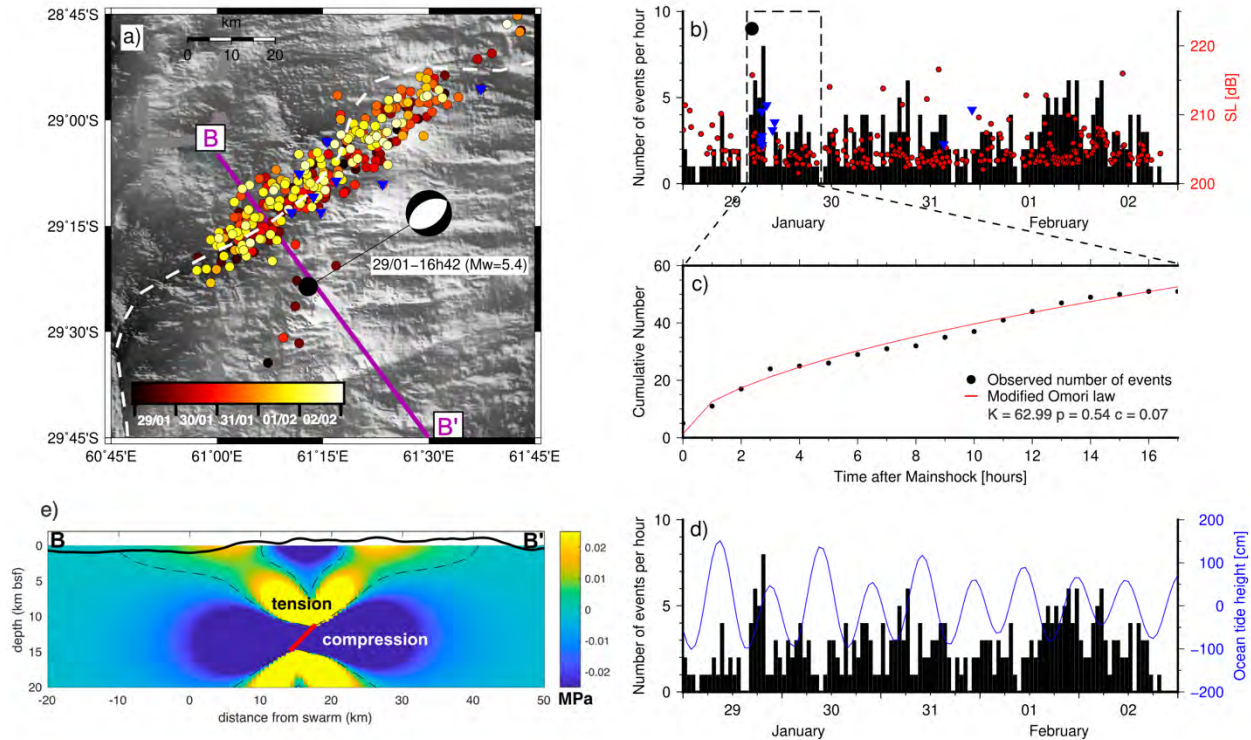
1020 **Figure 6 - Spatio-temporal distribution of events:** Month-wise temporal distribution of events
 1021 between June 2016 and March 2017. The dashed line shows the SWIR axis. The hot color scale
 1022 denotes the origin time of the events from start to end of each of the individual months. Number
 1023 of events per month (Nbr) are given in the upper right corner individually. Beach-ball represents
 1024 the focal mechanisms of the events that occurred in individual months (from the GCMT catalog).
 1025 Note that all the focal mechanisms are parallel to the SWIR axis except for the last one in February
 1026 2017 (parallel to the Melville TF).



1027

1028 **Figure 7 - 14th of December 2016 sequence 9:** a) Spatio-temporal distribution of the events
 1029 between December 13-06:00 and December 16-06:00. Beach-ball represents the normal faulting
 1030 focal mechanism of the only event in the GCMT catalog (December 15-01:29, Mw = 5.2). The
 1031 dashed line shows the SWIR axis. b) Histogram of number of events per hour in black color and
 1032 SLs of events in red circles. The dashed rectangle marks the temporal outline for the selection of
 1033 events to compute modified Omori's law. c) Black dots show the hourly cumulative number of
 1034 events between December 14 and 15, and the red curve shows the modified Omori's law fit with
 1035 the fitting parameters. d) Histogram of number of events per hour in black color vs the ocean tide
 1036 height in blue color. The higher seismicity rate coinciding with the high tide is marked in a gray
 1037 rectangle. e) Projection of the cluster of T-wave radiating points (red circles) at the seafloor depth
 1038 along A-A' profile (green line in a)). Yellow arrow represents schematic upwelling dikes beneath
 1039 the clustered events. The extent of the vertical axis (dashed line) below 10 km is tentative as we
 1040 do not know the depth of the dike.

1041



1042

1043 **Figure 8 - 29th of January 2017 sequence 12:** a) Spatio-temporal distribution of the events
 1044 between January 29 and February 02, 2017. Beach-ball represents the normal faulting focal
 1045 mechanism of the strongest event that started the sequence on January 29-16:42 (Mw = 5.4). The
 1046 dashed line shows the SWIR axis. b) Histogram of number of events per hour in black color. Red
 1047 circles and blue triangles show the SLs of T-waves and impulsive events, respectively. The dashed
 1048 rectangle is the temporal outline of the selection of events used to compute a modified Omori's
 1049 law. c) Black dots show the hourly cumulative number of events inside the dashed rectangle in b)
 1050 and the red curve shows the modified Omori's law fit and its fitting parameters. d) Histogram of
 1051 number of events per hour in black color vs the ocean tide height in blue color. e) Schematic
 1052 section (along B-B') showing the plausible geometry of a fault (red) located SE of the ridge axis
 1053 and the horizontal stress change in MPa caused by a Mw=5.4 normal slip event (18 cm of dip-slip
 1054 on a 5.1 x 5.1 km square patch embedded in an elastic half-space with Young's modulus and
 1055 Poisson's ratio 100 GPa and 0.25, respectively). The yellow color indicates that this active fault
 1056 set the ridge axis in an extensional regime that probably allowed a dike emplacement in the valley.